Quantum Dot–Peptide–Fullerene Bioconjugates for Visualization of *in Vitro* and *in Vivo* Cellular Membrane Potential

Okhil K. Nag[†,○], **Michael H. Stewart**[‡,○], **Jeffrey R. Deschamps**[†], **Kimihiro Susumu**[‡,#], **Eunkeu Oh**[‡,#], **Vassiliy Tsytsarev**[¶,□], **Qinggong Tang**[¶], **Alexander L. Efros**[§], **Roman Vaxenburg**[▽], **Bryan J. Black**[⊥], **YungChia Chen**[†], **Thomas J. O'Shaughnessy**[§], **Stella H. North**[†], **Lauren D. Field**[†,¶], **Philip E. Dawson**[∥], **Joseph J. Pancrazio**[⊥], **Igor L. Medintz**[†], **Yu Chen**[¶], **Reha S. Erzurumlu**[□], **Alan L. Huston**[‡], and **James B. Delehanty**[*,†]

[†]Center for Bio/Molecular Science and Engineering, Code 6900

[‡]Optical Sciences Division, Code 5600

[§]Materials and Science and Technology Division, Code 6300, U.S. Naval Research Laboratory, Washington, D.C. 20375, United States

[∥]Department of Chemistry, The Scripps Research Institute, La Jolla, California 92037, United States

[⊥]Department of Bioengineering, University of Texas at Dallas, Richardson, Texas 75080, United States

[#]Sotera Defense Solutions, Columbia, Maryland 21046, United States

[¶]Fischell Department of Bioengineering, University of Maryland, College Park, Maryland 20742, United States

[□]Department of Anatomy and Neurobiology, University of Maryland School of Medicine, Baltimore, Maryland 21201, United States

[▽]Computational Materials Science Center, George Mason University, Fairfax, Virginia 22030, United States

Abstract

We report the development of a quantum dot (QD)–peptide–fullerene (C_{60}) electron transfer (ET)-based nanobioconjugate for the visualization of membrane potential in living cells. The bioconjugate is composed of (1) a central QD electron donor, (2) a membrane-inserting peptidyl

[*]**Corresponding Author** james.delehanty@nrl.navy.mil.
[○]O. K. Nag and M. H. Stewart contributed equally.

linker, and (3) a C_{60} electron acceptor. The photoexcited QD donor engages in ET with the C_{60} acceptor, resulting in quenching of QD photoluminescence (PL) that tracks positively with the number of C_{60} moieties arrayed around the QD. The nature of the QD-capping ligand also modulates the quenching efficiency; a neutral ligand coating facilitates greater QD quenching than a negatively charged carboxylated ligand. Steady-state photophysical characterization confirms an ET-driven process between the donor–acceptor pair. When introduced to cells, the amphiphilic QD–peptide–C_{60} bioconjugate labels the plasma membrane by insertion of the peptide–C_{60} portion into the hydrophobic bilayer, while the hydrophilic QD sits on the exofacial side of the membrane. Depolarization of cellular membrane potential augments the ET process, which is manifested as further quenching of QD PL. We demonstrate in HeLa cells, PC12 cells, and primary cortical neurons significant QD PL quenching (F/F_0 of 2–20% depending on the QD–C_{60} separation distance) in response to membrane depolarization with KCl. Further, we show the ability to use the QD–peptide–C_{60} probe in combination with conventional voltage-sensitive dyes (VSDs) for simultaneous two-channel imaging of membrane potential. In *in vivo* imaging of cortical electrical stimulation, the optical response of the optimal QD–peptide–C_{60} configuration exhibits temporal responsivity to electrical stimulation similar to that of VSDs. Notably, however, the QD–peptide–C_{60} construct displays *20- to 40-fold* greater F/F_0 than VSDs. The tractable nature of the QD–peptide–C_{60} system offers the advantages of ease of assembly, large F/F_0, enhanced photostability, and high throughput without the need for complicated organic synthesis or genetic engineering, respectively, that is required of traditional VSDs and fluorescent protein constructs.

Graphical abstract
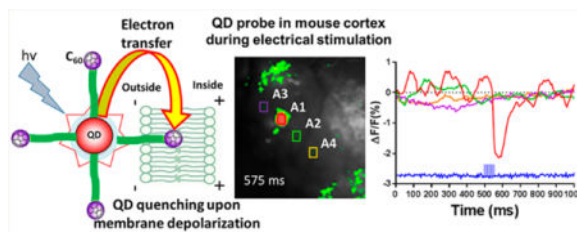
Keywords

quantum dot; peptide; fullerene; membrane potential; voltage; neuron; electron transfer

The nanoparticle (NP)–biological interface continues to be an intensely studied research frontier with a primary goal being the realization of functional hybrid nano-scale materials that possess enhanced or augmented capabilities.[1,2] Examples of such functionalities range from the use of the plasmonic thermal profile of gold nanoparticles (AuNPs) and nanoshells to specifically kill targeted cancer cells with incident light irradiation[3,4] to the employment of semiconductor nanocrystals or quantum dots (QDs) as a scaffold to facilitate the enhanced activity of appended enzymes.[5,6] Indeed, in both of these examples it is the inherent physicochemical properties of the NPs that facilitates the desired function. One arena in which the inherent properties of NPs have been predicted to make a significant impact is the real-time visualization of cellular membrane potential in electrically active

cells (*e.g.*, neurons and muscle cells). The primary goal of the United States' Brain Research through Advancing Innovative Neurotechnologies (BRAIN) Initiative is to create a functional map of the human brain connectome—all of the interconnections of the tens of billions of neurons in the brain—as a means to better understand the brain's function and dysfunction during disease and injury.[7] The European Commission's counterpart Human Brain Project seeks to replicate this brain activity map *in silico*.[8] Success here could enable the development of the next generation of diagnostic and therapeutic reagents for the treatment of a range of brain pathologies. One of the key questions that has been raised, however, is whether or not the neuroscience community possesses the proper tools capable of visualizing the activity of thousands of cells simultaneously while maintaining single-cell resolution.[9–12]

Much of the driving force for this stems from the inherent limitations of currently available tools and techniques for the imaging/recording of membrane potential from large numbers of cells.[13] For example, patch clamp, long the gold standard laboratory technique for recording and controlling membrane potential, is invasive, and it is limited to the interrogation of single cells.[14] Microelectrode-based techniques are similarly invasive and record membrane potential extracellularly, which prohibits single-cell resolution.[15] Fluorescence-based materials such as voltage-sensitive dyes (VSDs)[16] and fluorescent protein constructs[12] suffer from small changes in photoluminescence (PL) intensity ($\Delta F/F_0$), limited photostability, toxicity, or the requirement that cells be genetically manipulated to express the sensing construct. Further, Ca^{2+}-sensitive fluorescent constructs measure intracellular Ca^{2+} release that occurs hundreds of milliseconds after the action potential and, thus, lack temporal resolution.[17] One of the more promising genetically encoded voltage sensors are those based on archaerhodopsin, which display large PL changes (~1% $\Delta F/F_0$ per mV) and can be used combinatorially with other spectrally resolvable opsin channel actuators for all-optical simultaneous stimulation and recording.[18,19] Despite these advances, significant interest has arisen in the potential for NP materials to address some of the aforementioned critical issues.[20]

One particular class of NPs under consideration for the optical imaging of membrane potential are QDs, fluorescent materials synthesized on the nanoscale (<10 nm diameter) that exhibit quantum confinement. These nanocrystalline materials possess a number of photophysical attributes that make them ideal for imaging modulations in membrane potentials. These include QDs' (1) bright, stable PL coupled with nanosecond fluorescence lifetimes, (2) quantum confined Stark effect in response to an electric field,[21,23] (3) ability to be appended onto[24,25] or localized in[26] the plasma membrane bilayer, (4) large two-photon action cross sections that make them ideal for deep tissue imaging,[27,28] (5) ability to engage in efficient Förster resonance energy transfer (FRET)[29,30] and electron transfer (ET) processes,[31,32] and (6) low toxicity when implemented with experimental brain platforms.[33–36]

Several reports, both theoretical[37] and experimental,[21–23] support the notion that QDs can function as voltage-sensitive probes. Indeed, recent work from our group showed the ability of photoexcited quasi-type II QDs (QDs with spatial segregation of electron–hole (e–h) pairs) to track, with excellent time-resolved fidelity, the millisecond voltage trace of a

simulated firing cortical neuron.[38] Yet, studies demonstrating the use of plasma membrane-inserted QDs for voltage sensing remain scant.[39] This is largely due to the critical technical challenge of partitioning QDs coated with hydrophobic surface ligands *into* the ~4 nm thick aliphatic region of the plasma membrane without perturbing membrane integrity or the function of membrane channel proteins responsible for maintaining membrane potential.[2,26]

To overcome this technical hurdle, here we have designed QD–peptide–electron acceptor bioconjugates that obviate the need for direct insertion of the QD into the membrane bilayer. In the construct, a central hydrophilic QD (electron donor) serves as a scaffold for the self-assembly of multiple copies of a peptide–C_{60} fullerene conjugate (electron acceptor). This work builds on our previous observation that such QD–peptide–C_{60} conjugates engage in efficient ET-based quenching of QD PL that tracks with the number of peptide–C_{60} moieties displayed around the QD.[31] The helix-forming peptide that appends the C_{60} to the QD is designed to facilitate membrane insertion such that the hydrophobic C_{60} is buried within the lipid bilayer of the membrane while the hydrophilic QD is localized on the extracellular face of the exofacial leaflet of the plasma membrane. Upon depolarization of the membrane potential, the basal rate of ET from the photoexcited QD electron donor to the fullerene acceptor is enhanced, resulting in the further quenching of QD PL, the magnitude of which tracks with the increasing potential of the cell's plasma membrane (Figure 1C).

We present here the detailed photophysical analysis of this QD–peptide–C_{60} system both outside the cellular environment and when interfaced with the plasma membrane of cultured cell lines and primary neurons *in vitro* and in live mice *in vivo*. Our data clearly demonstrates that the efficiency of quenching of QD PL by the C_{60} electron acceptor is governed by the number of peptide–C_{60} conjugates arrayed around the central QD and the nature of the hydrophilic QD-capping ligand. In HeLa cells, the optimal QD–peptide–C_{60} construct exhibits a ~20% F/F_0 upon membrane depolarization, which is comparable to a commercially available fluorescein–aniline photoinduced electron transfer voltage imaging probe under the same conditions. In primary mouse cortical neurons, the QD–peptide–C_{60} construct exhibits a F/F_0 of ~7%. Importantly, cellular viabilities of >90% are observed in these studies, demonstrating minimal perturbation of cellular physiology. Finally, we employ the optimal QD–peptide–C_{60} probe for the real-time imaging of cortical electrical stimulation in live mice. Here, the fluorescence response of the QD–peptide–C_{60} probe exhibits temporal responsivity comparable to standard VSDs, yet with F/F_0 values that are *20- to 40-fold greater* than those reported for VSDs.

RESULTS AND DISCUSSION

Rationale for QD–Peptide–C_{60}-Based Membrane Potential Sensing Scheme

Our goal in this study was to design voltage-sensitive QD bioconjugates that engage in ET and can be interfaced with the plasma membrane of living cells such that membrane depolarization modulates ET, resulting in an optical readout. Specifically, depolarization of membrane potential results in a decrease in QD PL that tracks the transition from the resting state to the depolarized state (*vide infra*). Figure 1A shows schematically the design of the QD–peptide–C_{60} bioconjugate system and the three peptide variants used herein. The QD serves as the central scaffold onto which the peptidyl sequences (referred to as JBD1, JBD2,

and JBD3) are self-assembled using metal affinity coordination of the N-terminal His_6 motif to the QD surface.[40] By virtue of their alanine/leucine-rich nature, the peptides are designed to be helix-forming to promote membrane insertion.[41–43] Each peptidyl sequence expresses a unique lysine residue for the covalent attachment of one C_{60} electron acceptor per peptide *via* EDC chemistry. Peptide JBD1, with its lysine residue attachment point most proximal to the His_6 QD binding domain, positions the C_{60} closest to the QD surface upon assembly (QD–C_{60} surface-to-surface distance (ssd), ~10 Å). Peptide JBD3, which bears a nine-proline repeat that adopts a type II helical conformation,[44–46] positions the C_{60} most distal from the QD surface (ssd, ~42 Å). JBD2 positions the C_{60} at an intermediary distance from the QD (ssd, ~24 Å). See SI Table S1 for additional physicochemical properties of the peptides used herein.

Two variations of hydrophilic QD-capping ligand provide flexibility in terms of mediating colloidal stability in aqueous media while allowing the peptide's membrane inserting domain to extend from the QD surface. As evidenced by molecular modeling (Figure 1B), the shorter dihydrolipoic acid (DHLA) ligand (~11 Å extended length) affords maximal extension of the attached C_{60} beyond the ligand layer while providing colloidal stability at slightly basic pH.[47–49] The longer PEGylated (68 Å nm extended length) DHLA–PEG_{750}–OMe ligand, which terminates in a methoxy group, avails stability over a wide pH range,[50,51] but the longer extended length increases hydrodynamic volume while reducing the accessibility of the peptide–C_{60} to the surrounding aqueous environment. As shown in Figure 1C, the full QD–peptide–C_{60} ensemble is predicted to interface with the outer leaflet of the plasma membrane such that the peptide–C_{60} portion of the conjugate is embedded in the lipophilic bilayer. In this configuration, the photoexcited QD serves as the electron donor and is engaged in ET with the C_{60} moiety, a potent electron acceptor.[52,53] At resting membrane potential (~−70 mV) the differential positive charge of the outer membrane leaflet supports radiative recombination of photoexcited electrons and holes within the QD, resulting in bright QD luminescence. Upon membrane depolarization, however, photoexcited electrons from the QD are preferentially attracted to the C_{60} acceptor, resulting in quenching of QD PL.

For this study we prepared two samples of core/multishell QDs: (i) CdSe/CdS/ZnS and (ii) CdSe/CdS/CdZnS/ZnS QDs with emission maxima centered at 605 and 625 nm, respectively. Both QD samples are classified as quasi-type II QDs in which there is spatial separation between the e–h charge carriers such that photoexcited electrons should delocalize into the surrounding CdS layer. The outermost ZnS shell passivates the core to minimize surface defects and maintain QD quantum yield while simultaneously providing a surface for assembly of the His_6-bearing peptides by the ratiometric metal-affinity coordination as described previously.[54]

Characterization of QD–Peptide–C_{60} Bioconjugates

The successful covalent attachment of the C_{60} to each of the peptides was confirmed by spectroscopy (SI Figure S1). The peptides alone displayed only modest absorption in the 250–300 nm spectral window. By contrast, the peptide–C_{60} conjugates showed significant absorbance across the 250–350 nm spectral range, consistent with the absorbance of the C_{60}

fullerene.[55] The His$_6$-mediated assembly of the peptide C_{60} conjugates to the QD surface was characterized by dynamic light scattering (DLS) (SI Table S2). This analysis showed the concomitant increase in the hydrodynamic diameter of the QD coupled with a decrease in the diffusion coefficient when 30 copies of each peptide–C_{60} species were assembled onto the QD surface. Not surprisingly, the hydrodynamic diameter of the 605 nm QDs (13.8 nm) was larger than the hard diameter determined by transmission electron microscopy (TEM) (8.2 nm, SI Figure S2), as it includes contributions from the ligand capping layer and solvation sphere. Comparable results confirming successful assembly of the peptide–C_{60} to the surface of the 625 nm emitting QDs were also obtained. These results are consistent with our extensive previously published work showing the controlled, ratiometric assembly of His-tagged peptides and proteins to the QD surface and the long-term stability of the formed bioconjugates in cellular environments.[25,27,48,49,56–58]

Steady-State Photophysical Characterization of QD–Peptide–C_{60} Bioconjugates

Having confirmed our ability to controllably form QD–peptide–C_{60} bioconjugates, we next characterized the efficiency of the QD–peptide–C_{60} ET system using CdSe/CdS/ZnS QD (605 nm emission) as the electron donor. This emission window (along with the 625 nm QD) was chosen specifically to ensure that photoexcited ET from the QD donor to the C_{60} fullerene acceptor was more favorable than FRET. We have shown previously that while both ET and FRET processes between the QD donor and C_{60} acceptor are possible, the use of QDs whose emission is tuned to the 600–630 nm window significantly favors ET processes over FRET.[31] Steady-state QD PL quenching data were collected as a function of increasing numbers of peptide–C_{60} (*i.e.*, valence) arrayed around the central 605 nm QD capped with DHLA ligands. As evidenced in Figure 2A–C, across all three peptide–C_{60} species, the quenching efficiency tracked directly with the number of peptide–C_{60} assembled onto the QD scaffold. These results are consistent with our previous studies where the addition of increasing numbers of peptide–C_{60} allows for the iterative "tuning" of the quenching of QD PL.[31] Notably, control experiments in which the 605 nm DHLA-capped QDs were assembled with non-C_{60} peptides showed no significant quenching of QD PL. Additional control experiments to assess the quenching of the QDs by free C_{60} in solution (at a ratio of 20 C_{60}/QD) showed negligible quenching of QD PL, consistent with previous observations.[31] These data confirm the necessity for attachment of the C_{60} to the QD surface *via* the peptide linker to mediate efficient quenching.

In the case of the three peptide–C_{60} species under investigation here, maximal quenching occurred as the peptide valence approached ~60 peptides–C_{60}/QD. While this peptide valence is slightly under the maximum number of peptides predicted to be able to assemble to the 605 nm QD surface (~100 ± 20 peptides),[59] clearly a peptide valence of ~60 facilitated maximal quenching. Similar trends in QD PL quenching efficiency were observed for 605 QDs capped with DHLA–PEG$_{750}$–OMe ligands (Figure 2D, SI Figure S3). The modulation in PL intensity can be described by the relationship

$$\frac{I_{PL}(p)}{I_{PL}(0)} = \frac{1}{1 + pQY(\tau_r/\tau_e)}$$

where $I_{PL}(p)$ and $I_{PL}(0)$ are the PL of the QD in the presence and absence of peptide–C_{60}, respectively, p is the number of peptide–C_{60} assembled onto the QD surface, QY is the quantum yield of the QD in the absence of peptide–C_{60}, τ_r is the radiative decay time of the exciton in the QD, and τ_e is the time of electron transfer from the QD donor to the C_{60} acceptor (see the SI for equation derivation). In these steady-state experiments we observed no significant dependence of QD PL quenching efficiency on the QD–C_{60} separation distance, suggesting that in solution the peptide–C_{60} interacts similarly with the QD surface across all three peptide–C_{60} conjugates. This strongly suggests that in the aqueous environment under which the steady-state PL data were collected, the peptides adopt a less structured conformation that allows the C_{60} moiety to approach very near the QD surface regardless of the peptide sequence. In the presence of biological membranes, however, the peptides adopt a more rigid helical structure that maintains the QD–C_{60} separation distance predicted by modeling. This is consistent with the behavior of the peptides in the presence of liposomal membranes as confirmed by circular dichroism analysis (*vide infra*).

Interestingly, in comparison to DHLA-capped QDs, the overall magnitude of quenching observed for the PEG-capped QDs was significantly greater. Consider again the data at the peptide–C_{60}/QD valence of ~40. At this ratio on PEG-capped QDs, QD PL quenching efficiency ranged from ~83% (JBD1-C_{60}) to ~70% (JBD3-C_{60}), corresponding to increases of 33% and 35%, respectively, in the quenching efficiency of these same peptides in the context of DHLA-capped QDs. It is likely that the carboxyl functions on the DHLA ligands played a key role in these observed differences. At the pH 8.5 conditions under which these experiments were performed, the carboxyl groups would be predominantly ionized and would likely abrogate the rate of ET between the QD and the C_{60} *via* electrostatic shielding. In contrast, the uncharged PEGylated ligand system would likely not elicit this effect. This trend continued for DHLA– and DHLA–PEG_{750}–OMe-capped QDs with emis sion centered at 625 nm (SI Figure S4), demonstrating that the C_{60}-induced PL quenching operated consistently across QD platforms. It is also worth noting the structural and "excluded-volume" roles played by the PEG ligands in this context. Previous studies have implicated the role of PEGylated ligands in mediating conformational changes in peptide structure when assembled onto the QD surface, which can alter peptide persistence length,[44,60] resulting in shorter QD–C_{60} separation distances than those predicted by modeling. These effects likely contribute to the enhanced quenching of the QD by the C_{60} in the context of the PEG-capped QDs observed herein.

To confirm that the observed peptide–C_{60}-induced QD PL quenching was dominated by non-FRET processes (*i.e.*, ET), a wavelength-dependent quenching analysis was performed on the steady-state PL data. This analysis determines the magnitude of the wavelength dependence in QD quenching in QD donor–acceptor FRET systems, which is a hallmark of FRET systems that employ the QD as donor.[61] We previously used this analysis to confirm that FRET was the predominant energy transfer process in QD–peptide–osmium bioconjugates.[62] Herein, we performed this analysis on the QD–peptide–C_{60} ensembles (~30 peptides assembled/QD) and found that the QD quenching was wavelength-independent for all three JBD peptide species when assembled on DHLA or DHLA–PEG_{750}–OMe 605 nm QDs (SI Figure S5). Indeed, the flat slopes of the quenching efficiency plots coupled with the nearly symmetrical unquenched and quenched spectra

confirmed this. This is not surprising given the fact that in the 605 nm spectral window of the QD, the absorbance of the C_{60} is negligible and does not afford any appreciable energy transfer from the QD donor to C_{60} acceptor.[31] Further, the overlap integral between the 605 nm QD donor and C_{60} acceptor is minimal ($J = 1.16 \times 10^{-14}$ cm^3 M^{-1}) compared to lower wavelength emitting QDs.[31] Cumulatively, these data strongly suggest that ET is the dominant mechanism in the observed QD PL quenching.

Characterization of Membrane Binding of Peptide–C_{60} and QD–Peptide–C_{60} Conjugates

Having established the ET-based nature of QD quenching by the C_{60}, we next characterized the interaction of the peptide, peptide–C_{60}, and QD–peptide–C_{60} conjugates with the plasma membrane of living cells. The peptides used in this study were designed to insert into biological membranes by virtue of their alanine/leucine-rich sequence, which promotes helix stabilization.[41] To begin, we first characterized the unconjugated peptides' (no C_{60}) secondary structure alone in solution and in the presence of liposomal vesicles as analyzed by circular dichroism (CD). Peptides JBD2 and JBD3 were selected for this analysis, as the JBD2 sequence is nearly identical to JBD1 (except for the relocation of the internal lysine residue to the C-terminus and its replacement with leucine) and JBD3 contains a nine-proline repeat predicted to form a type II proline helix.[45] The CD spectra for peptides JBD2 and JBD3 and the accompanying tabulated results are shown in SI Figures S6 and S7, respectively. Here, we looked for clear trends showing an increasing percentage of a-helical content of the peptide when in the presence of liposomes compared to when the peptide was in phosphate-buffered saline (PBS) buffer alone. Indeed, for both peptides an increase in a-helical content was observed. For peptide JBD3, the increase in helical structure was less pronounced but still notable. Nonetheless, for both peptides, helical character was the only value for which an increase was observed, consistent with the peptides' adoption of a helical conformation in the presence of biological membranes. Similar observations have been made for other alanine-leucine-rich peptides.[41,63]

Next, we determined the membrane-inserting behavior of the peptide–C_{60} conjugates. To accomplish this, immunocyto-chemistry using a C_{60}-specific primary monoclonal antibody was performed to probe the interaction of the His$_6$-bearing JBD peptides and JBD–peptide–C_{60} conjugates with the membrane of A549 (adenocarcinomic human alveolar epithelial) cells. The primary antibody was probed with a secondary antibody–gold NP conjugate followed by silver staining to visualize the presence of the gold NP in the formed immunocomplex. As presented in the micrographs in Figure 3A and quantitatively in Figure 3B, the magnitude of the normalized silver staining intensity clearly tracked with the presence of the C_{60} moiety compared to the nonconjugated peptide. These data, together with the CD data showing helix formation in the presence of liposomes and the well-documented propensity of the C_{60} carbon allotrope to partition into biological membranes,[64–66] gave us great confidence that the His$_6$-tagged peptide–C_{60} conjugate would append hydrophilic coated QDs to the outer leaflet of the plasma membrane by virtue of its membrane-inserting properties.

To confirm the latter, we performed membrane labeling studies in A549 cells to determine the efficiency with which the self-assembled 605 nm QD–peptide–C_{60} bioconjugates

decorated the plasma membrane. As evidenced by Figure 3C and D, we observed robust, bright membrane labeling immediately after 10 min of incubation of 20 nM QDs (20 JBD–C_{60} peptides/QD) with the cell monolayers. The pH of the DPBS incubation buffer was adjusted to 7.9 to facilitate enhanced colloidal stability of the DHLA-capped QDs. The labeling was highly efficient (confirmed by confocal microscopy) with 70% (QD–JBD2–C_{60}) to 91% (QD–JBD1–C_{60}) of cells positive for membrane labeling. Cells probed with QD–JBD3–C_{60} conjugates showed a labeling efficiency of 81%. This labeling morphology remained membranous for at least 30 min with minimal endocytosis of the QDs. Comparable membranous labeling was obtained with peptide/QD ratios of >20 (data not shown). DHLA-capped QDs bearing no peptide showed minimal nonspecific binding to the cell monolayers (<10% of the signal of that for QD with peptide) over the same incubation time course. The QDs capped with DHLA–PEG_{750}–OMe ligands showed no significant binding whether or not they were decorated with peptide–C_{60} conjugates (data not shown). These observations are consistent with the important role of PEG ligands and coatings in minimizing nonspecific binding of a myriad of NPs both *in vitro* and *in vivo*.[67–69] Cumulatively, these data confirmed the successful membrane labeling with the QD-DHLA–peptide–C_{60} conjugates, setting up their use as optical probes for monitoring modulations in membrane potential.

In Vitro Characterization of the Fluorescence Response of QD–Peptide–C_{60} Conjugates to Membrane Depolarization

Having confirmed the successful membrane labeling of cells with the QD–DHLA–peptide–C_{60} conjugates, we next sought to ascertain the optical response of the probes to changes in membrane potential. We employed HeLa cells for this purpose, as our initial depolarization experiments on A549 cells using a commercial voltage-sensitive probe (FluoVolt) did not show any significant membrane depolarization response upon addition of 140 mM KCl. The addition of extracellular isotonic 140 mM KCl induces cells into a sustained depolarized state, and it has been used in a wide array of studies for the membrane depolarization of multiple cell types.[39,70–73] For these studies, 605 nm DHLA-capped QDs appended with 20 copies of JBD–C_{60} peptides were used. Not only did initial binding studies confirm excellent membrane labeling at this peptide valence, but this peptide/QD ratio also corresponded to ~35% quenching of steady-state QD PL, allowing for further quenching upon membrane depolarization.

Figure 4A shows a representative example of the fluorescence intensities at resting potential (2.5 mM KCl) and after membrane depolarization (by addition of 140 mM KCl) in HeLa cells labeled with QD–DHLA–JBD1–C_{60} conjugates. Upon depolarization, a notable decrease in fluorescence intensity was observed for all three QD–peptide–C_{60} conjugates with distinct differences observed among the three probes. Figure 4B shows the quantified fluorescence intensities of all three QD–peptide–C_{60} conjugates pre- and post-depolarization. The average percent fluorescence decreases (F/F_0 ± standard error of the mean (SEM)) were determined to be QD–JBD1–C_{60}, 20 ± 2% (41 cells queried); QD–JBD2–C_{60}, 12 ± 2% (52 cells); and QD–JBD3–C_{60}, 2 ± 1% (76 cells). Upon addition of 140 mM KCl, the membrane potential of HeLa cells is expected to rise from ~−50 mV to ~0 mV.[74] Accordingly, the percent fluorescence decreases per mV we observed here correspond

to estimated values of 0.40%, 0.24%, and 0.04% for JBD1, JBD2, and JBD3, respectively. The PL modulations in response to membrane depolarization observed here are consistent with those predicted by modeling the effects of changes in membrane potential on the electron tunneling efficiency in the QD–peptide–C_{60} conjugates (see the SI). Control experiments with HeLa cells labeled with QD–DHLA–JBD1 peptide (no C_{60}; 20 peptides per QD) showed less than 3% decrease in QD PL upon depolarization (SI Figure S8).

For comparison, Figure 4B also shows the response of the fast-response VSD FluoVolt, which displayed a fluorescence increase as expected (F/F_0 of 21% ± 2% (39 cells; 0.41% F/F_0 per mV)). Reported values of F/F_0 per mV for this dye range from 0.1% to 0.48% in patch-clamped cortical neurons and HEK cells, respectively,[75] values to which the QD–peptide–C_{60} conjugates reported here compare well. Relative to other fast-response VSDs (*e.g.*, ANEPPS dyes (0.1% F/F_0 per mV[76]); RH-1691 (0.01% F/F_0 per mV[77])) the fluorescence responses of the QD–peptide–C_{60} conjugates are significantly higher. The slow-response dibutylbarbituric-based VSD oxonol B438 exhibited a fluorescence increase of 64% (30 cells, 1.3% F/F_0 per mV). Despite its rather large F/F_0, oxonol B438 does not remain membrane-resident like other VSDs; it enters cells upon depolarization, where it binds to intracellular proteins and membranes, resulting in the influx of more dye and an increase in fluorescence.[78] Thus, it was used here primarily as a positive control indicator of successful membrane depolarization.

The relative magnitude of the depolarization-induced fluorescence changes observed for the three QD–peptide–C_{60} conjugates generally tracked inversely with increasing QD–C_{60} separation distance predicted by modeling (Figure 1B). This points to the important role played by the separation distance between the QD and C_{60} in mediating differential responsivity to changes in membrane potential, particularly when the QD–peptide–C_{60} complex is interfaced with the plasma membrane. In this context, the lipid environment of the plasma membrane likely plays a critical structural role in maintaining peptide persistence length and optimal QD–C_{60} separation distance in the hydrophobic bilayer.[79] It also strongly suggests that the loading conditions used consistently resulted in the proper orientation of the QD–DHLA–peptide–C_{60} complex in the plasma membrane wherein the hydrophilic QD is located on the cell surface and the hydrophobic peptide–C_{60} portion of the bioconjugate is buried within the aliphatic portion of the plasma membrane bilayer.

Importantly, the interfacing of the QD–DHLA–peptide–C_{60} conjugates with HeLa cells had minimal impact on their cellular viability. MTS proliferation assays were performed on HeLa cells incubated with QDs alone, JBD1–C_{60} peptide, or the full QD–DHLA–JBD1-C_{60} conjugate under the labeling conditions described in the Methods section. None of these materials induced significant toxicity, with viabilities of >85–90% noted in all cases (SI Figure S9). We also confirmed the successful labeling and biocompatibility of the QD–DHLA–JBD1–C_{60} conjugates using cultured networks of mouse cortical neurons (SI Figure S10). Following labeling of networks with the QD–DHLA–JBD1–C_{60} conjugates, cellular viabilities of >94% as compared to unlabeled control were determined by live/dead staining (five cultures and eight imaged regions of interest). These findings are consistent with previous studies detailing the largely innocuous nature of QD bioconjugates in biological

systems[48,49,56,80,81] and points to improvements in cellular viability relative to other organic voltage-sensitive dyes that are known to significantly impact cellular homeostasis.[82,83]

We further demonstrated the utility and flexibility of the QD–DHLA–JBD1–C_{60} conjugate for imaging membrane potential by performing a series of two-color depolarization experiments where the VSD oxonol B438 (green channel) and the QD conjugate (red channel) were used combinatorially to provide dual-channel visualization of membrane depolarization in HeLa cells (Figure 5). Here, upon KCl-induced depolarization, a ~21% decrease in QD conjugate PL coupled with a concomitant increase in oxonol B438 emission was noted. Comparable results were obtained in PC12 (rat adrenal medulla pheochromocytoma) cells (SI Figure S11). Notably, the presence of the oxonol fluorophore did not abrogate the function of the QD–peptide–C_{60} probe. This dual-channel format was also replicated in cultured monolayers of mouse primary cortical neurons where the QD PL was quenched ~7% upon depolarization, coupled with a corresponding ~5-fold increase in the emission of the oxonol probe (Figure 6). In addition to its demonstrated utility across multiple cell lines and primary cells, the narrow, red-shifted emission profile of the QD–peptide–C_{60} probe (SI Figure S12) avails direct two-color membrane potential imaging that has heretofore necessitated complicated deconvolution or ratiometric imaging due largely to the broad emission profiles of voltage-sensitive dyes.[84,85] Further, the simultaneous, differential PL responses of the oxonol (PL "on") and QD (PL "off") probes are easily discernible using standard filter sets.

In Vivo Characterization of the Fluorescence Response of QD–Peptide–C_{60} Conjugates to Cortical Brain Function

Given their significant photostability and large two-photon action cross sections, one of the very attractive applications of voltage-sensitive QD-based probes is the real-time imaging of *in vivo* brain function. To assess the sensitivity and temporal responsivity of our probes, we performed a series of cortical brain function imaging experiments in anesthetized B6 mice. Solutions of QD–JBD1–C_{60} (or control samples of QD–JBD1 (no C_{60}) or QDs alone) were injected into multiple regions of the right or left parietal cortex (SI Figure S13) followed by the region selective introduction of electrical stimulation (100 μA) from a bipolar tungsten electrode. To reduce noise and to assess the ability of the QD–peptide–C_{60} probe to respond to repetitive rounds of stimulation, optical signals were averaged over 50 successive trials in each animal tested. In each trial, the stimulus consisted of seven pulses (each 3 ms duration at 200 Hz, 12 s between each trial). Figure 7A shows the relevant time-resolved optical images collected from mouse cortex injected with QD–DHLA–JBD1–C_{60} conjugates. The temporal fluorescence intensity profiles of four regions of interest (ROIs) were queried before, during, and after the stimulus (575 ms frame expanded in Figure 7B for clarity). Note that the responding ROI (A1) is located proximal to one of the stimulating electrodes, while the nonresponsive ROIs are distal from the inserted electrode. As evidenced by the plots in Figure 7C, ROI A1 responded nearly immediately upon application of the stimulus and displayed maximal fluorescence decrease (F/F_0 = ~2.1%) at ~100 ms after stimulation onset. The response decayed upon removal of the stimulation, returning to baseline within 80–100 ms after removal of the applied stimulation. The variability of the response of the conjugate was also assessed across multiple animals, where the average percent PL response

across three animals (±SEM) was 2.1 ± 0.05 (SI Figure S14). Panels D and E in Figure 7 present the time-resolved fluorescence responses of mice injected with two control constructs: QD–JBD1 peptide (no C_{60}, panel D) and QDs alone (panel E), respectively (full data in SI Figure S12). Clearly, these two materials were nonresponsive to the applied stimulation, demonstrating the necessity of the full ensemble QD–peptide–C_{60} donor–acceptor conjugate for function.

In comparison to popular *in vivo* VSDs under these same experimental conditions, the QD–JBD1–C_{60} probe compares well in terms of its responsivity dynamics. For example, the so-called "blue dyes" RH-795 ($\lambda_{em\ max.}$ = 695 nm) and RH-1691 ($\lambda_{em\ max.}$ = 675 nm) are specifically designed to have minimal light scattering and be less sensitive to contamination from hemodynamic components of the vascular system.[82,86] These dyes respond optically within ~10 ms to applied electrical stimulation and return to baseline within 50–100 ms,[77] comparable to the QD–JBD1–C_{60} probe. However, the QD–JBD1–C_{60} conjugate system responds with a *20- to 40-fold larger* F/F_0 than the RH dyes (which typically exhibit F/F_0 values of only ~0.05–0.1%).[77] Clearly the QD–peptide–C_{60} probe offers significant improvement in signal strength with no sacrifice in temporal responsivity.

CONCLUSIONS

The desire to map the functional connectome of the human brain to better diagnose and treat brain injury and disease has necessitated the development of new imaging modalities that afford capabilities beyond currently available techniques and materials. Currently employed approaches for the *in vitro* or *in vivo* monitoring/imaging of neuronal cell activity (*e.g.*, action potentials) rely on patch clamp or fluorescent dyes/protein constructs and are limited by their lack of throughput, susceptibility to photobleaching, intracellular instability, or the need for the generation of transfected cells or transgenic animals.[13] Ideally, next-generation optical probes to circumvent these issues would possess most, if not all, of the following criteria: (1) optical responsivity to biologically relevant electric field strengths, (2) bright, stable PL for long-term imaging, (3) the ability to be targeted specifically and noninvasively to neurons across multiple experimental platforms (monolayer, tissue slice, and *in vivo* whole animal), (4) large two-photon action cross sections that avail deep tissue imaging, and (5) the ability to engage in efficient energy or charge transfer with nanosecond lifetime. Clearly, the realization of the above attributes requires an understanding of new functional hybrid materials and how to integrate them, with fine control, with cells, tissues, and organisms.

Taking these desired criteria into account, here we set out to build on our previous body of work where we showed the utility of QD bioconjugates in a number of applications with implications for neuronal cell imaging. These include the use of QD–peptide assemblies for the specific labeling of the plasma membrane in monolayer cultured cells,[24,25] the targeted labeling of neurons in tissue slices,[34,35] the *in vivo* tracking of brain development,[36] and the use of QD-coated patch pipets for multiphoton excitation-assisted deep-tissue visualization of live mouse electrophysiology.[33] These demonstrations, coupled with our previous work that showed the ability of QD–fullerene donor–acceptor systems to engage in efficient ET,[31]

motivated us to ascertain whether this ET system could be used for the real-time visualization of changes in membrane potential in live cells.

In this work, we designed a QD–peptide–C_{60} bioconjugate system wherein each of the three components plays a pivotal role. The core/shell QD is specifically designed to be of the type II configuration to promote spatial segregation of electron–hole charge carriers. This configuration was selected to promote enhanced sensitivity to applied electric fields, as we have reported previously.[38] The C_{60} is an efficient electron acceptor that quenches the PL of the photoexcited QD quantitatively as a function of the number of C_{60} acceptors assembled on the QD surface.[31] Finally, the alanine/leucinerich peptide bridge serves to append the C_{60} acceptor at discrete fixed distances while also mediating membrane insertion as confirmed by CD analysis and immunostaining. Steady-state PL quenching analysis confirmed that the efficiency of QD quenching was intimately dependent on the number of peptide–C_{60} acceptors arrayed around the central QD donor. This is consistent with ET theory and has been observed in donor–acceptor systems where the peptide plays the role of functional spacer and facilitates ET *via* tunneling.[87,88] In contrast to the work of Virkki *et al.*,[32] who studied the QD quenching efficiency of C_{60} attached directly to the capping ligand, our approach here provides finer control over the number of C_{60}s in the ensemble bioconjugate.

The nature of the ligand played a critical role in the quenching efficiency in the QD–C_{60} donor–acceptor system, as has been reported elsewhere in the literature for other QD-based ET systems.[89–91] The shorter, negatively charged DHLA ligand mediated a moderate degree of QD quenching, while for the same peptide/ratio combination the quenching induced by the uncharged DHLA–PEG_{750}–OMe ligand was significantly higher. In this context, it is likely that the negative charges on the DHLA ligands abrogate the efficient quenching of the QD PL. The Weiss group made similar observations in their studies of electron exchange between PbSe QDs and a negatively charged anthraquinone where the introduction of increasing numbers of charged 6-mercaptohexanoate ligands resulted in a concomitant decrease in the rate of ET.[92]

Just as the ligand coating influenced the QD quenching efficiency, it was also a critical determinant of the interaction of the assembled QD–peptide–C_{60} conjugates with cells. DHLA–PEG-capped QDs assembled with any of the three JBD–C_{60} conjugates showed no detectable QD binding to the plasma membrane. Molecular modeling strongly suggested the steric shielding of the peptide–C_{60} conjugates in the context of this ligand coating. DHLA-capped QDs, however, presented the peptide–C_{60} conjugate beyond the ligand shell and extending from the QD surface. These observations are consistent with previous reports showing the effect of the capping ligand layer on the display and packing of peptides and proteins on the QD surface when assembled *via* the His_n-based metal affinity strategy used herein.[59,93] It is fortuitous in our case that the DHLA ligand coating that affords more efficient binding of the QD–peptide–C_{60} bioconjugates to the plasma membrane also mediates only a moderate degree of QD quenching. The intermediary degree of quenching in this ligand system (~35% quenching at 20 JBD1 peptides/QD) avails a sufficient dynamic range for further QD quenching upon depolarization of membrane potential.

We functionally demonstrated the utility of the QD–peptide–C_{60} system for the imaging of membrane potential changes in cultured HeLa and PC12 cells and in primary cortical neurons. In these systems, we showed the compatibility of the QD–peptide–C_{60} probe with standard voltage-sensitive dyes for two-color combinatorial membrane potential imaging. We further showed their ability to be used as photostable labeling probes in networks of cortical neurons cultured on microelectrode arrays (MEAs). Finally, *in vivo* imaging of cortical electrical stimulation functionally demonstrated the superior imaging capability of the QD–peptide–C_{60} probe compared to traditional VSDs, where a 20- to 40-fold improvement in F/F_0 was realized with no sacrifice in responsivity.

Previous reports have demonstrated the ability to interface QD-based ET constructs with live cells for imaging applications. Medintz *et al.* used QDs engaged in ET with a peptide–dopamine conjugate self-assembled to the QD surface to monitor intracellular pH changes in real time.[58] In those studies, the QDs were physically microinjected into the cellular cytosol to visualize drug-induced alkalosis. In the present report, the QD–peptide–C_{60} bioconjugate spans the outer leaflet of the plasma membrane, and the starting degree of quenching of the photoexcited QD by the C_{60} moiety at resting potential can be modulated by the number of C_{60} acceptors arrayed around the central QD donor.

The QD–peptide–C_{60} system we describe here offers several distinct advantages over VSDs and genetically encoded voltage-sensitive fluorescent protein constructs. First, the F/F_0 values observed are larger than commonly employed VSDs (*vide supra*). Second, its modular nature affords facile assembly and tractability that cannot be readily achieved with organic dyes that require complicated synthesis and purification schemes.[75,85,94,95] Third, the QD quenching efficiency is tunable and easily controlled through rational peptide design as demonstrated here. Fourth, as the system employs QDs in the >600 nm emission window as electron donors, cellular autofluorescence is minimized. Of particular note is the large two-photon action cross sections of QDs (often 10^3–10^4 times greater than organic dyes),[28,96] which could allow deeper tissue imaging combined with voltage sensing.[33] Finally, in contrast to previous reports that have used QDs as optical voltage-sensing probes,[39] our approach described here is not dependent on the insertion of the QDs into the membrane bilayer. This is a considerable challenge given the hard diameter of QDs (typically 5–10 nm) relative to the 4 nm expanse of the aliphatic portion of the bilayer. Membrane-partitioning QDs require hydrophobic coatings, and their delivery depends on the use of fusogenic delivery vesicles for membrane insertion.[26] We expect that the QD–peptide–C_{60} system described here will find great utility in an array of voltage-sensing schemes. Given the significantly higher photostability and two-photon action cross sections of QDs compared to VSDs, we anticipate the expanded use of the QD–peptide–C_{60} constructs described herein for deeper tissue imaging of *in vivo* brain function.

METHODS/EXPERIMENTAL

Materials

All chemicals were purchased from Sigma-Aldrich (St. Louis, MO, USA) and used as received unless otherwise mentioned. Dulbecco's phosphate buffered saline (DPBS), 4-(2-hydroxyethyl)-1-piperazineethanesulfonic acid (HEPES, 1 M), Dulbecco's modified Eagle

medium (DMEM), modified Eagle medium (MEM), fetal bovine serum (FBS), DMEM containing 25 mM HEPES (DMEM–HEPES), antibiotic–antimycotic, DiBAC$_4$(3) (bis(1,3-dibutylbarbituric acid)trimethine oxonol (B438)), and FluoVolt membrane potential kit were purchased from Life Technologies (Grand Island, NY, USA). Primary fullerene mouse monoclonal IgG and goat anti-mouse polyclonal–gold nanoparticle conjugate were obtained from Santa Cruz Biotechnology (Santa Cruz, CA, USA). 1,2-Dipalmitoyl-*sn*glycero-3-phosphocholine was from Avanti Polar Lipids (Alabaster, AL, USA).

Quantum Dots

CdSe/CdS/ZnS and CdSe/CdS/CdZnS/ZnS QDs with emission maxima at 605 and 625 nm, respectively, were synthesized according to previously published procedures.[97–100] DHLA and DHLA–PEG$_{750}$–OMe were prepared according to established protocols.[49,51,99,101] A two-step ligand exchange procedure was used to coat these QDs with DHLA or DHLA–PEG$_{750}$–OMe ligands, adopted from our previous work for the transfer of QDs to water with pyridine-appended polymers.[102] Briefly, the QDs (5 nmol) were precipitated with acetone and centrifuged at 3500 rpm for 5 min, and the supernatant was discarded. The QD pellet was mixed with ethanol (0.5 mL), chloroform (0.3 mL), and 2-(2-aminoethoxy)-ethanol (0.15 mL) and then heated at 60 °C for 1 h under nitrogen with stirring to form a clear solution. After cooling to room temperature, the QDs were precipitated with a mixture of ethyl acetate, 2-propanol, and hexanes. The QDs were centrifuged at 3500 rpm for 5 min, and the supernatant discarded. The QD pellets were then mixed with ethanol (0.5 to 1 mL) and the desired ligand at approximately 30 000 equiv of ligand per QD. The mixture was sealed under nitrogen and stirred at 60 °C overnight. The QDs were then purified according to published protocols.[103] DHLA and DHLA–PEG$_{750}$–OMe coated QDs were stored in sodium tetraborate (4–5 mM) and DI water solutions, respectively, in the dark at 4 °C.

Transmission Electron Microscopy of QDs

Structural characterization of asprepared QDs was carried out using a JEOL 2200-FX analytical high-resolution transmission electron microscope with a 200 kV accelerating voltage. Samples for TEM were prepared by spreading a drop (5–10 μL at a concentration of ~1 μM) of the filtered QD dispersion onto an ultrathin carbon support film on a 300 mesh Au grid (Ted Pella, Inc.) and letting it dry. Individual particle sizes were measured using a Gatan Digital Micrograph (Pleasanton, CA, USA). Average sizes along with standard deviations were extracted from analysis of ~100 QDs.

Peptide–C$_{60}$ Conjugates

Peptides were labeled with C$_{60}$ and purified according to the procedure detailed in ref 31 with slight modifications. Briefly, peptide (1 mg, 1 equiv), C$_{60}$-pyrrolidine tris-acid (Sigma-Aldrich) (6 equiv), and *N*-hydroxysuccinimide (84 equiv) were placed in a 20 mL scintillation vial with 2 mL of 95% DMSO/H$_2$O. Triethylamine (8 equiv) was added to the mixture with stirring. After a few minutes *N,N*′-diisopropylcarbodiimide (66 equiv) was added, and the mixture was stirred overnight (~16 to 20 h) at room temperature in the absence of light. To isolate the C$_{60}$-labeled peptide, 0.5 mL of DI water and 2.5 mL of Ni^{2+}-nitrilotriacetic acid agarose resin (Qiagen, Valencia, CA, USA) was added to the reaction mixture and stirred for 1–2 h. The resin was then filtered on a glass frit and washed with

DMSO (~6 × 7 mL aliquots, or until the filtrate was colorless) and then DI water (~4 × 7 mL aliquots). The C_{60}-labeled peptide was then eluted from the resin using an imidazole (600–900 mM) solution in 90% DMSO/H_2O (~4 × 1 mL aliquots). The combined filtrate was desalted on a preprimed oligonucleotide purification cartridge (OPC) and dried to a pellet.[40] After desalting, the bound peptide was eluted with neat acetonitrile (~4 × 0.1 mL aliquots) and then dried. The peptide pellet was dissolved in DMSO, quantified by UV–vis spectrophotometry (C_{60} absorbance at 350 nm, 34 300 M^{-1} cm^{-1}), and then stored at −20 °C. The conjugation of the C_{60} to the peptide was confirmed by differential absorbance spectroscopy using unconjugated peptide as a reference.

Molecular Modeling of QD–Peptide–C_{60} Conjugates

All models were created using tools in UCSF Chimera, version 1.4.1. Energy minimization was carried out in Chimera using built-in features including ANTECHAMBER (version 1.27) and the AM1-BCC method of calculating charges.[104] The model of the C_{60} fullerene was constructed from the structure of (η^5-pentaphenyl-C_{60}fullerene)-(η^5-cyclopentadienyl)iron carbon disulfide.[105] The covalently attached phenyl groups were removed from the fullerene using the tools in Chimera, and the resulting model was energy minimized as described above. The C_{60} fullerene was further modified to contain a bridging group on the region formerly occupied by the phenyl groups. A model for peptide JBD2 (see Figure 1 for peptide sequences) was first created in Chimera. On the basis of prior work the His_6 region was modeled with an extended conformation, which is consistent with the four to six coordination bonds the His_6 tail forms with the QD surface. The remaining portion of the peptide was modeled as a helix based on both modeling and similarity to other short peptides of know conformation. Following initial peptide folding the peptide model was energy minimized using tools in Chimera. The helical conformation of the AALAAWAALAAAAALAAAK region was verified using Mobyle[106] and PSIPRED.[107] The models for the C_{60} fullerene and peptide linker were joined, and the full model was energy minimized. In a similar manner the JBD3 peptide containing a Pro_9 segment was built in Chimera. The helical region of peptide JBD2 was extended by inserting an Ala-Pro_9 segment just before the His_6 QD binding region to yield the full JBD3 sequence. The Pro_9 was constrained to be helical based on prior work.[44,108] Lastly a model for the JBD1 sequence was constructed in Chimera with residues 1–20 constrained to be α-helical and the His_6 region extended. In this model the C_{60} was attached to the ε-amino group in the internal lysine residue. All models were docked to the surface of the QD with a diameter of 100 Å with an 11 Å DHLA layer on the QD surface. Comparable models were generated where the QD was coated with a DHLA–PEG_{750}–OMe ligand layer (~33 Å thick). Molecular graphics images were produced using the UCSF Chimera package from the Resource for Biocomputing, Visualization, and Informatics at the University of California, San Francisco (supported by NIH P41 RR-01081).

Self-Assembly of Quantum Dot–Peptide Conjugates for Optical Characterization

The QD–peptide–C_{60} conjugates were prepared *via* self-assembly using the conditions described previously.[31] Briefly, the frozen, concentrated C_{60}-labeled peptide solutions (in DMSO) were thawed, sonicated, and then used to form diluted peptide stock solutions in DMSO (~10 μM). The following is an example for preparing the conjugates with DHLA–

and PEG$_{750}$–OMe-coated QDs. First, QDs (~10 pmol, 0.26 μM) in 14 mM sodium tetraborate buffer (pH ~8.5) were mixed with DMSO, and then appropriate volumes of C$_{60}$-labeled peptide stock solutions (10 μM) were added to achieve the desired peptide/QD ratio with a final volume of 110 μL. The initial volume of DMSO added was adjusted for each ratio of peptide/QD to achieve a final DMSO content of 65% (v/v). The final QD concentration was 90 nM. These solutions were mixed and assembled overnight before analysis. Successful self-assembly of the peptide–C$_{60}$ conjugates to the QD surface was confirmed by measuring particle size and distribution *via* DLS using a ZetaSizer NanoSeries equipped with a HeNe laser source (λ = 633 nm) (Malvern Instruments Ltd., Worcestershire, UK) and analyzed using Dispersion Technology Software (DTS, Malvern Instruments Ltd.).

Optical Characterization of QD–Peptide–C$_{60}$ Conjugates

Steady-state photoluminescence measurements were performed on a Tecan Infinite M1000 fluorescence multifunction plate reader. Electronic absorption spectra were collected on an HP 8453 diode array spectrophotometer (Agilent Technologies, Santa Clara, CA, USA).

Liposome Synthesis

Liposomes composed of 1,2-dipalmitoyl-*sn*glycerol-3-phosphocholine phospholipids were prepared through thin film hydration. The phospholipids were dissolved in chloroform to a final concentration of ~10–20 mM. The lipids were then placed in a round-bottom flask, and the solvent was removed overnight by Rotovap under vacuum to produce a thin lipid film. The lipids were rehydrated in ~5 mL of warmed PBS (preheated to ~45 °C) for 1 h. The lipid suspension was agitated by shaking for 30 min and then placed in a bath sonicator for a minute to produce liposomal vesicles.

Analysis of Peptide Structure by Circular Dichroism

CD experiments were carried out using a Jasco J-815 CD spectrometer (Jasco, Easton, MD, USA). A peptide concentration of 5 μM was used for CD measurements. CD spectra were recorded in phosphate buffer, pH 7.0, in the presence or absence of liposomes (~250 μM lipids). Wavelength scans were performed from 190 to 260 nm in a thermally controlled (20 °C) quartz cell having a 0.1 cm path length. Each CD spectrum was the average of three scans done at a scan rate of 50 nm/ min using a data pitch of 1 nm, data integration time of 8 s, bandwidth of 1 nm, and a scan speed of 50 nm per min. The background spectrum (buffer only in the cuvette) was measured first, followed by that of the peptide or peptide/liposome solution. Collected CD data were normalized, and the ellipticity value (θ, in mdeg) was converted to standard units of deg·cm^2/dmol (designated as [θ]) using [θ] = θ/(path length in mm × molar concentration of peptide × number of residues). Data on the molar ellipticity as a function of wavelength that were obtained from the CD scans were deconvoluted using the SP-22X algorithm and analyzed using the CONTIN/LL software packages to yield the predicted percentages of secondary structural components. These programs analyze the ellipticity values at each wavelength and compare them with a library of proteins with known secondary structure to estimate the percentages of the various components.

Cell Culture

A549 and HeLa cells (ATCC, Manassas, VA, USA) were cultured in DMEM and MEM, respectively. Each basal medium was amended to contain 10% FBS, 1× antibiotic–antimycotic, and 1 mM sodium pyruvate to yield the complete growth medium formulation. All cellular delivery/staining experiments were performed using cells between passages 5 and 15. In general, cells were seeded to 35 mm culture dishes fitted with 14 mm #1.0 cover glass inserts (MatTek Corp., Ashland, MA, USA) at a density of ~7×10^4 cells/mL (total 3 mL/dish). The dishes were precoated with fibronectin (10–20 μg/mL) in DPBS before adding the cell suspension, and the cells were cultured for 24 h prior to use in labeling experiments.

For primary neuronal cultures, glass dishes were pretreated with 50 μg/mL poly-D-lysine (Sigma-Aldrich) by placing 50 μL drops in the center of the dishes overnight, rinsing twice with DI water, and allowing to air-dry. Next, 50 μL drops of 20 μg/mL laminin (Sigma-Aldrich) in DPBS (without Ca^{2+} or Mg^{2+}; Thermo Fisher Scientific Inc., Waltham, MA, USA) were placed at the center of the dishes for 1 h, then removed, and the dishes air-dried. [109] E18 murine cortices were obtained commercially (BrainBits LLC, Springfield, IL, USA) or surgically isolated and cultured as previously described.[107] Briefly, embryonic cortices were surgically dissected, minced, and placed in serum-free DMEM containing 20 U/mL papain (Sigma) in papain activation buffer (1.1 mM EDTA, 67 μM mercaptoethanol, and 5 mM L-cysteine) and 200 U/mL DNase (Thermo Scientific) for 20 min at 37 °C. Enzymatically dissociated tissue was then triturated using a fire-polished Pasteur pipet until the suspension appeared uniform (20–30 times). Following trituration, the cells and dissociation solution were centrifuged at 250g for 5 min, and the resulting pellet was resuspended in 1 mL of complete cell medium (high-glucose DMEM + Glutamax, 2% B27, 8 μg/mL L-ascorbic acid, 5% horse serum, 5% fetal bovine serum) for cell counting. Additional medium was then added to obtain a cell concentration of 1×10^6/mL. An aliquot (50 μL) of cell solution was added to the center of each well and kept at 37 °C, 10% CO_2, and 90% humidity for approximately 2 h to facilitate cell adhesion, then flooded with an additional 1 mL of complete medium. Cortical cultures underwent 50% medium exchanges every 48 h prior to QD labeling and live/dead staining experiments. Following 7 days in culture, complete cell medium was replaced with serum-free medium to cease the proliferation of non-neuronal cells.

Determination of Membrane-Binding Efficiency of Peptides and Peptide–C$_{60}$ Conjugates by Silver Staining

Growth media was removed, and A549 cell monolayers and the cells were washed with DMEM–HEPES. The cells were then incubated with 5–10 μM peptide or peptide–C_{60} conjugates for 10–15 min at 37 °C. Following washing with DMEM–HEPES, the cells were fixed with paraformaldehyde (3.7% in DPBS) for 15 min followed by permeabilization using 0.01% Triton/DPBS for 15 min at room temperature. Then the cells were washed again with DMEM–HEPES and incubated with mouse anti-C_{60} monoclonal Ab (3.3 μg/mL in 0.1% gelatin/DPBS) for 45 min at 37 °C followed by incubation with secondary goat anti-mouse (2 μg/mL in 0.1% gelatin/DPBS) for 45 min at 37 °C. The cells were washed with DMEM–HEPES and water and stained for 5 min using a silver staining/enhancer kit

(Sigma-Aldrich). A control sample without peptides was also prepared following the same procedure. The samples were imaged by differential interference contrast (DIC), and the degree of staining was quantified by selecting ROIs for individual cells using ImageJ software ver. 1.50i (National Institutes of Health, USA).

Preparation of QD–DHLA–Peptide–C$_{60}$ Complexes for Membrane Labeling and Depolarization Studies

The QD–DHLA–peptide–C$_{60}$ complexes were prepared by adding 2 μL of a 3 μM QD stock solution (final QD concentration 20 nM) to 297 μL of peptide solution (400 nM final concentration) in PBS (pH 7.9–8.2). The final QD:peptide–C$_{60}$ ratio was 1:20. The mixtures were incubated for 15 min at room temperature to form QD–peptide assemblies. The complexes were briefly centrifuged and used immediately to label cellular membranes.

Cellular Labeling with QD–DHLA–Peptide–C$_{60}$ Complexes

Complete growth medium was removed from cell monolayers, and the cells were washed with DMEM–HEPES. Solutions (typically ~150 μL) of QD–DHLA (20 nM QD) or QD–DHLA–peptide–C$_{60}$ complexes (20 nM QD appended with 20 peptides/QD; 400 nM peptide concentration) were incubated on the cells for 10–15 min at 37 °C followed by washing with DPBS. The cells were fixed with paraformaldehyde (3.7% in DPBS) for 15 min at room temperature, stored in 0.05% NaN$_3$/PBS at 4 °C, and imaged within 48 h. Live cell imaging during depolarization studies was performed as described below.

KCl Depolarization Studies

Depolarization experiments were performed on live HeLa, PC-12, and primary murine neuronal cells. The cells were labeled with QD–DHLA–peptide–C$_{60}$ complexes as described above. For comparison, two commercial voltage-sensitive probes were also studied: the slow response dye, oxonol (B438), or the fast response probe, FluoVolt. Cells were labeled with oxonol by incubation with 125 μL of 1 μM oxonol in DMEM–HEPES for 5 min at 4 °C. Labeling of cells with FluoVolt was done according to the manufacturer's supplied protocol. After staining cells were washed with DPBS. Live cell imaging solution (200 μL, Life Technologies) was added to cover the cell monolayers. Cells were imaged (*vide infra*) for florescence response to membrane depolarization induced by the addition of isotonic 140 mM KCl solution. In these experiments, 140 mM KCl was perfused into the culture dish over 3 min, and the KCl concentration was allowed to stabilize for another 2 min. Fluorescence was quantified at the beginning and end of this regimen. Fluorescence quantification of images was done using NIS-Elements AR 4.3 software (Nikon Co. Ltd., Tokyo, Japan) by sampling multiple RIOs in individual cells.

Microscopy

Imaging of fixed cell samples and live cell depolarization experiments was performed by DIC and confocal laser scanning microscopy using a Nikon A1RSi confocal microscope equipped with a 405 nm diode laser with fluorescence detection channels set to 500–550 nm (green) and 570–620 nm (red) with dichroic mirrors at 405/488/561/640 nm. All images were collected using a Plan Apo 60× objective. Laser power, PMT gain, and threshold for

each channel were held constant across different samples to allow for quantitative analysis. The confocal images were acquired as a *z*-stack comprising sequential/series optical *x–y* sections taken at 0.5–1.5 μm *z*-intervals using NIS-Elements AR 4.3 software (Nikon Co. Ltd., Tokyo, Japan). The images were processed for publication with Adobe Photoshop CS4 (ver. 11.0).

Cellular Proliferation Assays

The cytotoxicity of QDs and QD–peptide–C_{60} complexes was determined on HeLa cells using the CellTiter 96 Aqueous One Solution MTS cell proliferation assay (Promega, Madison, WI, USA). This assay is based upon the conversion of a tetrazolium substrate to a soluble formazan product by viable cells. HeLa cells were seeded to the wells of 96-well tissue culture plates ($\sim 5 \times 10^3$ cells/well). QDs and QD–peptide–C_{60} complexes were incubated on the cells for 15 min to emulate the labeling conditions used herein. After incubation, the materials were replaced with complete growth medium and the cells were cultured for 72 h. After this proliferation period, 20 μL of the tetrazolium substrate was added to each well, and color formation proceeded at 37 °C for 4h. The absorbance of the formazan product was read at 590 and 620 nm (for subtraction of nonspecific background absorbance) using a Tecan Infinite M1000 (Tecan, US) microtiter plate reader. Absorbance values with the background subtracted were reported as percent of control cell proliferation (degree of proliferation of cells in cell culture media only).

Cortical Neuron Live/Dead Assays

Live cell staining was carried out using Calcein AM (Thermo Fisher). Briefly, cells were washed three times in PBS and incubated in serum-free complete cell medium containing 2 μM Calcein AM at 37 °C for 10 min.

In Vivo Optical Recording of Cortical Brain Function

Experimental procedures were all in accordance with the National Institutes of Health guidelines for the care of experimental animals and an experimental protocol approved by the Animal Use and Care Committee of the University of Maryland School of Medicine. Imaging was performed on a total of five adult mice (B6 male and female, 25–30 g body weight, age 5–10 weeks): QD–JBD1–C_{60} (2 mice), QD–JBD1 (1 mouse), QD alone (2 mice). All animals were anesthetized with urethane (1.2 g/kg) and fixed on a stereotactic frame. A 3×3 mm section of the cranial bone above the left or right parietal cortex was removed using a dental drill. The exposed dural surface was cleaned with a hemostatic sponge and washed with artificial cerebral spinal fluid (ACSF). After craniotomy, 3–6 intracortical injections (0.5 μL each) of QD (1 μM QD) or QD–peptide solution (QDs assembled with 20 peptide/QD) were performed using a Nanojet II injector device fitted with a glass micropipet (20–50 μm diameter) mounted on a micromanipulator that allowed precise injections 0.3 mm below the dural surface. After injection the cortex was washed with ACSF, covered with high-density silicone oil, and sealed with a 0.1 mm thick cover glass to suppress brain pulsations caused by cardiovascular and respiratory movements. For imaging, the CCD camera was positioned above the recording area and directed such that its optical axis was perpendicular to the cortical surface. The focusing plane was set 100 μm below the dural surface. During recording, the imaging area of the cortex was illuminated

with a tungsten filament lamp (12 V, 100 WA, Zeiss) passed through an excitation filter (490 ± 30 nm) and a dichroic mirror at 575 nm. Imaging was performed through a tandem configuration of two 50 mm lenses, at a frame rate of 200 Hz, and recorded using a MiCAM-02 system (SciMedia, Costa Mesa, CA, USA).

For electrical stimulation, a bipolar tungsten electrode was introduced into the cortex at a depth of 0.1–0.2 mm. An electrical stimulus (100 μA) was computer-generated using an ISO-Flex stimulator (A.M.P.I., Israel) and consisted of seven pulses (each 3 ms duration, 100 Hz frequency). At the start of each optical recording, a grayscale image of the opened cortical region was captured and saved as a graphic file. Each experimental session consisted of 50 trials (500 frames/trial) with the electrical stimulus (one stimulus per trial) presented at the 100th frame (500 ms). The interval between trials was 12 s. Fluorescence changes were calculated as F/F_0 in ROIs using Brain Vision Analyzer (Brain Products GmbH, Germany). Images of areas activated by electrical stimulation were pseudocolored for publication.

Data analysis

The data were statistically analyzed by the univariate analysis of variance (ANOVA) using GraphPad Prism 6.01 software for Windows (La Jolla, CA, USA). For multiple comparisons, Bonferroni's *post hoc* test was applied. All average values were given ± standard error of mean unless otherwise mentioned. The acceptable probability for significance was $p < 0.05$.

Supplementary Material

Refer to Web version on PubMed Central for supplementary material.

Acknowledgments

References

1. Nel AE, Madler L, Velegol D, Xia T, Hoek EMV, Somasundaran P, Klaessig F, Castranova V, Thompson M. Understanding Biophysicochemical Interactions at the Nano-Bio Interface. Nat Mater. 2009; 8:543–557. [PubMed: 19525947]

2. Dennis AM, Delehanty JB, Medintz IL. Emerging Physicochemical Phenomena along with New Opportunities at the Biomolecular–Nanoparticle Interface. J Phys Chem Lett. 2016; 7:2139–2150. [PubMed: 27219278]

3. Lal S, Clare SE, Halas NJ. Nanoshell-Enabled Photothermal Cancer Therapy: Impending Clinical Impact. Acc Chem Res. 2008; 41:1842–1851. [PubMed: 19053240]

4. Bardhan R, Lal S, Joshi A, Halas NJ. Theranostic Nanoshells: From Probe Design to Imaging and Treatment of Cancer. Acc Chem Res. 2011; 44:936–946. [PubMed: 21612199]

5. Breger JC, Ancona MG, Walper SA, Oh E, Susumu K, Stewart MH, Deschamps JR, Medintz IL. Understanding How Nanoparticle Attachment Enhances Phosphotriesterase Kinetic Efficiency. ACS Nano. 2015; 9:8491–8503. [PubMed: 26230391]

6. Ding S, Cargill AA, Medintz IL, Claussen JC. Increasing the Activity of Immobilized Enzymes with Nanoparticle Conjugation. Curr Opin Biotechnol. 2015; 34:242–250. [PubMed: 25957941]

7. Weiss PS. President Obama Announces the BRAIN Initiative. ACS Nano. 2013; 7:2873–2874. [PubMed: 23607423]

8. The Human Brain Project. https://www.humanbrainproject.eu (accessed January 12, 2017).

9. Alivisatos AP, Chun M, Church, George M, Greenspan, Ralph J, Roukes, Michael L, Yuste R. The Brain Activity Map Project and the Challenge of Functional Connectomics. Neuron. 2012; 74:970–974. [PubMed: 22726828]

10. Andrews AM, Weiss PS. Nano in the Brain: Nano-Neuroscience. ACS Nano. 2012; 6:8463–8464. [PubMed: 23088783]

11. Antic SD, Empson RM, Knöpfel T. Voltage Imaging to Understand Connections and Functions of Neuronal Circuits. J Neurophysiol. 2016; 116:135–152. [PubMed: 27075539]

12. Storace D, Rad MS, Kang B, Cohen LB, Hughes T, Baker BJ. Toward Better Genetically Encoded Sensors of Membrane Potential. Trends Neurosci. 2016; 39:277–289. [PubMed: 27130905]

13. Peterka DS, Takahashi H, Yuste R. Imaging Voltage in Neurons. Neuron. 2011; 69:9–21. [PubMed: 21220095]

14. Sakmann, Ba, Neher, E. Patch Clamp Techniques for Studying Ionic Channels in Excitable Membranes. Annu Rev Physiol. 1984; 46:455–472. [PubMed: 6143532]

15. Rios G, Lubenov EV, Chi D, Roukes ML, Siapas AG. Nanofabricated Neural Probes for Dense 3-D Recordings of Brain Activity. Nano Lett. 2016; 16:6857–6862. [PubMed: 27766885]

16. Tsytsarev V, Liao LD, Kong KV, Liu YH, Erzurumlu RS, Olivo M, Thakor NV. Recent Progress in Voltage-Sensitive Dye Imaging for Neuroscience. J Nanosci Nanotechnol. 2014; 14:4733–44. [PubMed: 24757943]

17. Broussard GJ, Liang R, Tian L. Monitoring Activity in Neural Circuits with Genetically Encoded Indicators. Front Mol Neurosci. 2014; 7:1–17. [PubMed: 24574959]

18. Maclaurin D, Venkatachalam V, Lee H, Cohen AE. Mechanism of Voltage-Sensitive Fluorescence in a Microbial Rhodopsin. Proc Natl Acad Sci U S A. 2013; 110:5939–5944. [PubMed: 23530193]

19. Hochbaum DR, Zhao Y, Farhi SL, Klapoetke N, Werley CA, Kapoor V, Zou P, Kralj JM, Maclaurin D, Smedemark-Margulies N, Saulnier JL, Boulting GL, Straub C, Cho YK, Melkonian M, Wong GK-S, Harrison DJ, Murthy VN, Sabatini BL, Boyden ES, et al. All-Optical Electrophysiology in Mammalian Neurons Using Engineered Microbial Rhodopsins. Nat Methods. 2014; 11:825–833. [PubMed: 24952910]

20. Alivisatos AP, Andrews AM, Boyden ES, Chun M, Church GM, Deisseroth K, Donoghue JP, Fraser SE, Lippincott-Schwartz J, Looger LL, Masmanidis S, McEuen PL, Nurmikko AV, Park H, Peterka DS, Reid C, Roukes ML, Scherer A, Schnitzer M, Sejnowski TJ, Shepard KL, et al. Nanotools for Neuroscience and Brain Activity Mapping. ACS Nano. 2013; 7:1850–1866. [PubMed: 23514423]

21. Park K, Deutsch Z, Li JJ, Oron D, Weiss S. Single Molecule Quantum-Confined Stark Effect Measurements of Semiconductor Nanoparticles at Room Temperature. ACS Nano. 2012; 6:10013–10023. [PubMed: 23075136]

22. Empedocles SA, Bawendi MG. Quantum-Confined Stark Effect in Single CdSe Nanocrystallite Quantum Dots. Science. 1997; 278:2114–2117. [PubMed: 9405345]

23. Krauss TD, Brus LE. Electronic Properties of Single Semiconductor Nanocrystals: Optical and Electrostatic Force Microscopy Measurements. Mater Sci Eng, B. 2000; 69:289–294.

24. Delehanty JB, Blanco-Canosa JB, Bradburne CE, Susumu K, Stewart MH, Prasuhn DE, Dawson PE, Medintz IL. Site-Specific Cellular Delivery of Quantum Dots with Chemoselectively-Assembled Modular Peptides. Chem Commun. 2013; 49:7878–7880.

25. Boeneman K, Delehanty JB, Blanco-Canosa JB, Susumu K, Stewart MH, Oh E, Huston AL, Dawson G, Ingale S, Walters R, Domowicz M, Deschamps JR, Algar WR, DiMaggio S, Manono J, Spillmann CM, Thompson D, Jennings TL, Dawson PE, Medintz IL. Selecting Improved Peptidyl Motifs for Cytosolic Delivery of Disparate Protein and Nanoparticle Materials. ACS Nano. 2013; 7:3778–3796. [PubMed: 23710591]

26. Gopalakrishnan G, Danelon C, Izewska P, Prummer M, Bolinger PY, Geissbuhler I, Demurtas D, Dubochet J, Vogel H. Multifunctional Lipid/Quantum Dot Hybrid Nanocontainers for Controlled Targeting of Live Cells. Angew Chem, Int Ed. 2006; 45:5478–5483.

27. Clapp AR, Pons T, Medintz IL, Delehanty JB, Melinger JS, Tiefenbrunn T, Dawson PE, Fisher BR, O'Rourke B, Mattoussi H. Two-Photon Excitation of Quantum Dot-Based Fluorescence Resonance Energy Transfer and Its Applications. Adv Mater. 2007; 19:1921–1926.

28. Resch-Genger U, Grabolle M, Cavaliere-Jaricot S, Nitschke R, Nann T. Quantum Dots *Versus* Organic Dyes as Fluorescent Labels. Nat Methods. 2008; 5:763–775. [PubMed: 18756197]

29. Clapp AR, Medintz IL, Mauro JM, Fisher BR, Bawendi MG, Mattoussi H. Fluorescence Resonance Energy Transfer Between Quantum Dot Donors and Dye-Labeled Protein Acceptors. J Am Chem Soc. 2004; 126:301–310. [PubMed: 14709096]

30. Medintz IL, Pons T, Susumu K, Boeneman K, Dennis A, Farrell D, Deschamps JR, Melinger JS, Bao G, Mattoussi H. Resonance Energy Transfer Between Luminescent Quantum Dots and Diverse Fluorescent Protein Acceptors. J Phys Chem C. 2009; 113:18552–18561.

31. Stewart MH, Huston AL, Scott AM, Oh E, Algar WR, Deschamps JR, Susumu K, Jain V, Prasuhn DE, Blanco-Canosa J, Dawson PE, Medintz IL. Competition Between Förster Resonance Energy Transfer and Electron Transfer in Stoichiometrically Assembled Semiconductor Quantum Dot–Fullerene Conjugates. ACS Nano. 2013; 7:9489–9505. [PubMed: 24128175]

32. Virkki K, Demir S, Lemmetyinen H, Tkachenko NV. Photoinduced Electron Transfer in CdSe/ZnS Quantum Dot–Fullerene Hybrids. J Phys Chem C. 2015; 119:17561–17572.

33. Andrasfalvy BK, Galinanes GL, Huber D, Barbic M, Macklin JJ, Susumu K, Delehanty JB, Huston AL, Makara JK, Medintz IL. Quantum Dot-Based Multiphoton Fluorescent Pipettes for Targeted Neuronal Electrophysiology. Nat Methods. 2014; 11:1237–1241. [PubMed: 25326662]

34. Walters R, Kraig RP, Medintz I, Delehanty JB, Stewart MH, Susumu K, Huston AL, Dawson PE, Dawson G. Nanoparticle Targeting to Neurons in a Rat Hippocampal Slice Culture Model. ASN Neuro. 2012; 4:383–392. [PubMed: 22973864]

35. Walters R, Medintz IL, Delehanty JB, Stewart MH, Susumu K, Huston AL, Dawson PE, Dawson G. The Role of Negative Charge in the Delivery of Quantum Dots to Neurons. ASN Neuro. 2015; 7:1–12.

36. Agarwal R, Domowicz MS, Schwartz NB, Henry J, Medintz I, Delehanty JB, Stewart MH, Susumu K, Huston AL, Deschamps JR, Dawson PE, Palomo V, Dawson G. Delivery and Tracking of Quantum Dot Peptide Bioconjugates in an Intact Developing Avian Brain. ACS Chem Neurosci. 2015; 6:494–504. [PubMed: 25688887]

37. Marshall JD, Schnitzer MJ. Optical Strategies for Sensing Neuronal Voltage Using Quantum Dots and Other Semiconductor Nanocrystals. ACS Nano. 2013; 7:4601–4609. [PubMed: 23614672]

38. Rowland CE, Susumu K, Stewart MH, Oh E, Makinen AJ, O'Shaughnessy TJ, Kushto G, Wolak MA, Erickson JS, Efros AL, Huston AL, Delehanty JB. Electric Field Modulation of Semiconductor Quantum Dot Photoluminescence: Insights into the Design of Robust Voltage-Sensitive Cellular Imaging Probes. Nano Lett. 2015; 15:6848–6854. [PubMed: 26414396]

39. Molokanova E, B JA, Zhao W, Naasani I, Ignatius MJ, Treadway JA, Savtchenko A. Quantum Dots Move Beyond Fluorescence Imaging. Biophotonics Int. 2008:26–31.

40. Sapsford KE, Farrell D, Sun S, Rasooly A, Mattoussi H, Medintz IL. Monitoring of Enzymatic Proteolysis on a Electroluminescent-CCD Microchip Platform Using Quantum Dot-Peptide Substrates. Sens Actuators, B. 2009; 139:13–21.

41. Lyu PC, Sherman JC, Chen A, Kallenbach NR. Alpha-Helix Stabilization by Natural and Unnatural Amino Acids with Alkyl Side Chains. Proc Natl Acad Sci U S A. 1991; 88:5317–5320. [PubMed: 2052608]

42. Karle IL, Flippen-Anderson JL, Sukumar M, Balaram P. Helix Packing of Leucine-Rich Peptides: A Parallel Leucine Ladder in the Structure of Boc-Aib-Leu-Aib-Aib-Leu-Leu-Leu-Aib-Leu-Aib-OMe. Proteins: Struct, Funct, Genet. 1992; 12:324–330. [PubMed: 1579566]

43. Marqusee S, Robbins VH, Baldwin RL. Unusually Stable Helix Formation in Short Alanine-Based Peptides. Proc Natl Acad Sci U S A. 1989; 86:5286–5290. [PubMed: 2748584]

44. Gemmill KB, Díaz SA, Blanco-Canosa JB, Deschamps JR, Pons T, Liu HW, Deniz A, Melinger J, Oh E, Susumu K, Stewart MH, Hastman DA, North SH, Delehanty JB, Dawson PE, Medintz IL.

Examining the Polyproline Nanoscopic Ruler in the Context of Quantum Dots. Chem Mater. 2015; 27:6222–6237.

45. Rabanal F, Ludevid MD, Pons M, Giralt E. CD of Proline-Rich Polypeptides: Application to the Study of the Repetitive Domain of Maize Glutelin-2. Biopolymers. 1993; 33:1019–1028. [PubMed: 8343583]

46. Pujals S, Giralt E. Proline-Rich, Amphipathic Cell-Penetrating Peptides. Adv Drug Delivery Rev. 2008; 60:473–484.

47. Mattoussi H, Mauro JM, Goldman ER, Anderson GP, Sundar VC, Mikulec FV, Bawendi MG. Self-Assembly of CdSe-ZnS Quantum Dot Bioconjugates Using an Engineered Recombinant Protein. J Am Chem Soc. 2000; 122:12142–12150.

48. Bradburne CE, Delehanty JB, Boeneman Gemmill K, Mei BC, Mattoussi H, Susumu K, Blanco-Canosa JB, Dawson PE, Medintz IL. Cytotoxicity of Quantum Dots Used for *In Vitro* Cellular Labeling: Role of QD Surface Ligand, Delivery Modality, Cell Type, and Direct Comparison to Organic Fluorophores. Bioconjugate Chem. 2013; 24:1570–1583.

49. Delehanty JB, Medintz IL, Pons T, Brunel FM, Dawson PE, Mattoussi H. Self-Assembled Quantum Dot-Peptide Bio-conjugates for Selective Intracellular Delivery. Bioconjugate Chem. 2006; 17:920–927.

50. Susumu K, Uyeda HT, Medintz IL, Pons T, Delehanty JB, Mattoussi H. Enhancing the Stability and Biological Functionalities of Quantum Dots *via* Compact Multifunctional Ligands. J Am Chem Soc. 2007; 129:13987–96. [PubMed: 17956097]

51. Mei BC, Susumu K, Medintz IL, Delehanty JB, Mountziaris TJ, Mattoussi H. Modular Poly(Ethylene Glycol) Ligands for Biocompatible Semiconductor and Gold Nanocrystals with Extended pH and Ionic Stability. J Mater Chem. 2008; 18:4949–4958.

52. Haddon RC, Palmer RE, Kroto HW, Sermon PA. The Fullerenes: Powerful Carbon-Based Electron Acceptors [and Discussion]. Philos Trans R Soc, A. 1993; 343:53–62.

53. Guldi DM. Fullerenes: Three Dimensional Electron Acceptor Materials. Chem Commun. 2000:321–327.

54. Blanco-Canosa JB, Wu M, Susumu K, Petryayeva E, Jennings TL, Dawson PE, Algar WR, Medintz IL. Recent Progress in the Bioconjugation of Quantum Dots. Coord Chem Rev. 2014; 263–264:101–137.

55. Dong H, Zhu H, Meng Q, Gong X, Hu W. Organic Photoresponse Materials and Devices. Chem Soc Rev. 2012; 41:1754–1808. [PubMed: 22158983]

56. Delehanty JB, Bradburne CE, Boeneman K, Susumu K, Farrell D, Blanco-Canosa JB, Dawson G, Dawson PE, Medintz IL. Delivering Quantum Dot-Peptide Bioconjugates to the Cellular Cytosol: Escaping from the Endolysosomal System. Integr Biol. 2010; 2:265–277.

57. Medintz IL, Pons T, Delehanty JB, Susumu K, Brunel FM, Dawson PE, Mattoussi H. Intracellular Delivery of Quantum Dot-Protein Cargos Mediated by Cell Penetrating Peptides. Bioconjugate Chem. 2008; 19:1785–1795.

58. Medintz IL, Stewart MH, Trammell SA, Susumu K, Delehanty JB, Mei BC, Melinger JS, Blanco-Canosa JB, Dawson PE, Mattoussi H. Quantum-Dot/Dopamine Bioconjugates Function as Redox Coupled Assemblies for *In Vitro* and Intracellular pH Sensing. Nat Mater. 2010; 9:676–684. [PubMed: 20651808]

59. Prasuhn DE, Deschamps JR, Susumu K, Stewart MH, Boeneman K, Blanco-Canosa JB, Dawson PE, Medintz IL. Polyvalent Display and Packing of Peptides and Proteins on Semiconductor Quantum Dots: Predicted *Versus* Experimental Results. Small. 2010; 6:555–564. [PubMed: 20077423]

60. Kuznetsova I, Zaslavsky B, Breydo L, Turoverov K, Uversky V. Beyond the Excluded Volume Effects: Mechanistic Complexity of the Crowded Milieu. Molecules. 2015; 20:1377. [PubMed: 25594347]

61. Pons T, Medintz IL, Sykora M, Mattoussi H. Spectrally Resolved Energy Transfer Using Quantum Dot Donors: Ensemble and Single-Molecule Photoluminescence Studies. Phys Rev B: Condens Matter Mater Phys. 2006; 73:245302–245307.

62. Stewart MH, Huston AL, Scott AM, Efros AL, Melinger JS, Gemmill KB, Trammell SA, Blanco-Canosa JB, Dawson PE, Medintz IL. Complex Förster Energy Transfer Interactions Between

Semiconductor Quantum Dots and a Redox-Active Osmium Assembly. ACS Nano. 2012; 6:5330–5347. [PubMed: 22671940]

63. Ahmad A, Azmi S, Srivastava S, Kumar A, Tripathi JK, Mishra NN, Shukla PK, Ghosh JK. Design and Characterization of Short Antimicrobial Peptides Using Leucine Zipper Templates with Selectivity Towards Microorganisms. Amino Acids. 2014; 46:2531–2543. [PubMed: 25069749]

64. Ikeda A, Kiguchi K, Shigematsu T, Nobusawa K, Kikuchi J-i, Akiyama M. Location of [60]Fullerene Incorporation in Lipid Membranes. Chem Commun. 2011; 47:12095–12097.

65. Russ KA, Elvati P, Parsonage TL, Dews A, Jarvis JA, Ray M, Schneider B, Smith PJS, Williamson PTF, Violi A, Philbert MA. C60 Fullerene Localization and Membrane Interactions in RAW 2647 Immortalized Mouse Macrophages. Nanoscale. 2016; 8:4134–4144. [PubMed: 26866469]

66. Zhang S, Mu Y, Zhang JZH, Xu W. Effect of Self-Assembly of Fullerene Nano-Particles on Lipid Membrane. PLoS One. 2013; 8:e77436. [PubMed: 24204827]

67. Tong R, Kohane DS. New Strategies in Cancer Nano-medicine. Annu Rev Pharmacol Toxicol. 2016; 56:41–57. [PubMed: 26514197]

68. Kobayashi K, Wei J, Iida R, Ijiro K, Niikura K. Surface Engineering of Nanoparticles for Therapeutic Applications. Polym J. 2014; 46:460–468.

69. Jokerst JV, Lobovkina T, Zare RN, Gambhir SS. Nanoparticle PEGylation for Imaging and Therapy. Nanomedicine. 2011; 6:715–728. [PubMed: 21718180]

70. Macías W, Carlson R, Rajadhyaksha A, Barczak A, Konradi C. Potassium Chloride Depolarization Mediates CREB Phosphorylation in Striatal Neurons in an NMDA Receptor-Dependent Manner. Brain Res. 2001; 890:222–232. [PubMed: 11164788]

71. Levitan ES, Gealy R, Trimmer JS, Takimoto K. Membrane Depolarization Inhibits Kv1.5 Voltage-Gated K Channel Gene Transcription and Protein Expression in Pituitary Cells. J Biol Chem. 1995; 270:6036–6041. [PubMed: 7890735]

72. Obata T, Aomine M, Yamanaka Y. Potassium Chloride Depolarization Enhances MPP+-Induced Hydroxyl Radical Generation in the Rat Striatum. Brain Res. 2000; 852:488–491. [PubMed: 10678780]

73. Lindgren S. Effects of KCl-Induced Depolarization on the GABA Concentration in the Corpus Striatum and in the Substantia Nigra. J Neural Transm. 1986; 66:161–170. [PubMed: 3783143]

74. Zhang X, Jin Y, Plummer MR, Pooyan S, Gunaseelan S, Sinko PJ. Endocytosis and Membrane Potential Are Required for HeLa Cell Uptake of R.I.-CKTat9, a Retro-Inverso Tat Cell Penetrating Peptide. Mol Pharmaceutics. 2009; 6:836–48.

75. Woodford CR, Frady EP, Smith RS, Morey B, Canzi G, Palida SF, Araneda RC, Kristan WB, Kubiak CP, Miller EW, Tsien RY. Improved PeT Molecules for Optically Sensing Voltage in Neurons. J Am Chem Soc. 2015; 137:1817–1824. [PubMed: 25584688]

76. Loew LM, Cohen LB, Dix J, Fluhler EN, Montana V, Salama G, Wu JY. A Naphthyl Analog of the Aminostyryl Pyridinium Class of Potentiometric Membrane Dyes Shows Consistent Sensitivity in a Variety of Tissue, Cell, and Model Membrane Preparations. J Membr Biol. 1992; 130:1–10. [PubMed: 1469705]

77. Tsytsarev V, Premachandra K, Takeshita D, Bahar S. Imaging Cortical Electrical Stimulation *In Vivo*: Fast Intrinsic Optical Signal *Versus* Voltage-Sensitive Dyes. Opt Lett. 2008; 33:1032–1034. [PubMed: 18451977]

78. Epps DE, Wolfe ML, Groppi V. Characterization of the Steady-State and Dynamic Fluorescence Properties of the Potential-Sensitive Dye Bis-(1,3-Dibutylbarbituric Acid) Trimethine Oxonol (Dibac4(3)) in Model Systems and Cells. Chem Phys Lipids. 1994; 69:137–150. [PubMed: 8181103]

79. Liu LP, Li SC, Goto NK, Deber CM. Threshold Hydrophobicity Dictates Helical Conformations of Peptides in Membrane Environments. Biopolymers. 1996; 39:465–470. [PubMed: 8756523]

80. Wegner KD, Hildebrandt N. Quantum Dots: Bright and Versatile *In Vitro* and *In Vivo* Fluorescence Imaging Biosensors. Chem Soc Rev. 2015; 44:4792–4834. [PubMed: 25777768]

81. Nazarenus M, Zhang Q, Soliman MG, del Pino P, Pelaz B, Carregal-Romero S, Rejman J, Rothen-Rutishauser B, Clift MJD, Zellner R, Nienhaus GU, Delehanty JB, Medintz IL, Parak WJ. *In Vitro* Interaction of Colloidal Nanoparticles with Mammalian Cells: What Have We Learned Thus Far? Beilstein J Nanotechnol. 2014; 5:1477–1490. [PubMed: 25247131]

82. Grandy TH, Greenfield SA, Devonshire IM. An Evaluation of *In Vivo* Voltage-Sensitive Dyes: Pharmacological Side Effects and Signal-to-Noise Ratios after Effective Removal of Brain-Pulsation Artifacts. J Neurophysiol. 2012; 108:2931–2945. [PubMed: 22972958]

83. Mennerick S, Chisari M, Shu HJ, Taylor A, Vasek M, Eisenman LN, Zorumski CF. Diverse Voltage-Sensitive Dyes Modulate GABA(A) Receptor Function. J Neurosci. 2010; 30:2871–2879. [PubMed: 20181584]

84. Shynkar VV, Klymchenko AS, Duportail G, Demchenko AP, Mely Y. Two-Color Fluorescent Probes for Imaging the Dipole Potential of Cell Plasma Membranes. Biochim Biophys Acta, Biomembr. 2005; 1712:128–136.

85. Loew, LM. Design and Use of Organic Voltage Sensitive Dyes. In: Canepari, M., Zecevic, D., editors. Membrane Potential Imaging in the Nervous System: Methods and Applications. Springer New York; New York, NY: 2011. p. 13-23.

86. Grinvald A, Lieke EE, Frostig RD, Hildesheim R. Cortical Point-Spread Function And Long-Range Lateral Interactions Revealed by Real-Time Optical Imaging of Macaque Monkey Primary Visual Cortex. J Neurosci. 1994; 14:2545. [PubMed: 8182427]

87. Onuchic JN, Kobayashi C, Baldridge KK. Quantum Tunneling in Biological Reactions: The Interplay Between Theory and Experiments. J Braz Chem Soc. 2008; 19:206–210.

88. Marcus RA, Sutin N. Electron Transfers in Chemistry and Biology. Biochim Biophys Acta, Rev Bioenerg. 1985; 811:265–322.

89. Morris-Cohen AJ, Aruda KO, Rasmussen AM, Canzi G, Seideman T, Kubiak CP, Weiss EA. Controlling the Rate of Electron Transfer Between a Quantum Dot and a Tri-Ruthenium Molecular Cluster by Tuning the Chemistry of the Interface. Phys Chem Chem Phys. 2012; 14:13794–13801. [PubMed: 22588225]

90. Hines DA, Kamat PV. Quantum Dot Surface Chemistry: Ligand Effects and Electron Transfer Reactions. J Phys Chem C. 2013; 117:14418–14426.

91. Bley S, Diez M, Albrecht F, Resch S, Waldvogel SR, Menzel A, Zacharias M, Gutowski J, Voss T. Electron Tunneling from Colloidal CdSe Quantum Dots to ZnO Nanowires Studied by Time-Resolved Luminescence and Photoconductivity Experiments. J Phys Chem C. 2015; 119:15627–15635.

92. He C, Weinberg DJ, Nepomnyashchii AB, Lian S, Weiss EA. Control of the Redox Activity of PbS Quantum Dots by Tuning Electrostatic Interactions at the Quantum Dot/Solvent Interface. J Am Chem Soc. 2016; 138:8847–8854. [PubMed: 27341608]

93. Dennis AM, Sotto DC, Mei BC, Medintz IL, Mattoussi H, Bao G. Surface Ligand Effects on Metal-Affinity Coordination to Quantum Dots: Implications for Nanoprobe Self-Assembly. Bioconjugate Chem. 2010; 21:1160–1170.

94. Miller EW, Lin JY, Frady EP, Steinbach PA, Kristan WB, Tsien RY. Optically Monitoring Voltage in Neurons by Photo-Induced Electron Transfer Through molecular wires. Proc Natl Acad Sci U S A. 2012; 109:2114–2119. [PubMed: 22308458]

95. Huang YL, Walker AS, Miller EW. A Photostable Silicon Rhodamine Platform for Optical Voltage Sensing. J Am Chem Soc. 2015; 137:10767–10776. [PubMed: 26237573]

96. Fisher JAN, Salzberg BM, Yodh AG. Near Infrared Two-Photon Excitation Cross-Sections of Voltage-Sensitive Dyes. J Neurosci Methods. 2005; 148:94–102. [PubMed: 16129493]

97. Clapp AR, Goldman ER, Mattoussi H. Capping of Cdse-Zns Quantum Dots with DHLA and Subsequent Conjugation with Proteins. Nat Protoc. 2006; 1:1258–66. [PubMed: 17406409]

98. Snee PT, Chan YH, Nocera DG, Bawendi MG. Whispering-Gallery-Mode Lasing from a Semiconductor Nanocrystal/ Microsphere Resonator Composite. Adv Mater. 2005; 17:1131–1136.

99. Li JJ, Wang YA, Guo WZ, Keay JC, Mishima TD, Johnson MB, Peng XG. Large-Scale Synthesis of Nearly Monodisperse CdSe/CdS Core/Shell Nanocrystals Using Air-Stable Reagents *via* Successive Ion Layer Adsorption and Reaction. J Am Chem Soc. 2003; 125:12567–12575. [PubMed: 14531702]

100. Blackman B, Battaglia D, Peng XG. Bright and Water-Soluble Near Ir-Emitting Cdse/Cdte/ZnSe Type-II/Type-I Nano-crystals, Tuning the Efficiency and Stability by Growth. Chem Mater. 2008; 20:4847–4853.

101. Uyeda HT, Medintz IL, Jaiswal JK, Simon SM, Mattoussi H. Synthesis of Compact Multidentate Ligands to Prepare Stable Hydrophilic Quantum Dot Fluorophores. J Am Chem Soc. 2005; 127:3870–8. [PubMed: 15771523]

102. Susumu K, Oh E, Delehanty JB, Pinaud F, Gemmill KB, Walper S, Breger J, Schroeder MJ, Stewart MH, Jain V, Whitaker CM, Huston AL, Medintz IL. A New Family of Pyridine-Appended Multidentate Polymers As Hydrophilic Surface Ligands for Preparing Stable Biocompatible Quantum Dots. Chem Mater. 2014; 26:5327–5344.

103. Mei BC, Susumu K, Medintz IL, Mattoussi H. Polyethylene Glycol-Based Bidentate Ligands to Enhance Quantum Dot and Gold Nanoparticle Stability in Biological Media. Nat Protoc. 2009; 4:412–23. [PubMed: 19265800]

104. Wang J, Wang W, Kollman PA, Case DA. Automatic Atom Type and Bond Type Perception in Molecular Mechanical Calculations. J Mol Graphics Modell. 2006; 25:247–260.

105. Herber RH, Nowik I, Matsuo Y, Toganoh M, Kuninobu Y, Nakamura E. Mössbauer Spectroscopy of Bucky Ferrocenes: Lattice Dynamics and Motional Anisotropy of the Metal Atom. Inorg Chem. 2005; 44:5629–5635. [PubMed: 16060611]

106. Néron B, Ménager H, Maufrais C, Joly N, Maupetit J, Letort S, Carrere S, Tuffery P, Letondal C. Mobyle: A New Full Web Bioinformatics Framework. Bioinformatics. 2009; 25:3005–3011. [PubMed: 19689959]

107. Buchan DWA, Minneci F, Nugent TCO, Bryson K, Jones DT. Scalable Web Services for the PSIPRED Protein Analysis Workbench. Nucleic Acids Res. 2013; 41:349–357.

108. Adzhubei AA, Sternberg MJE. Left-Handed Polyproline-Ii Helices Commonly Occur in Globular-Proteins. J Mol Biol. 1993; 229:472–493. [PubMed: 8429558]

109. Knaack GL, Charkhkar H, Hamilton FW, Peixoto N, O'Shaughnessy TJ, Pancrazio JJ. Differential Responses to ω-agatoxin IVA in Murine Frontal Cortex and Spinal Cord Derived Neuronal Networks. NeuroToxicology. 2013; 37:19–25. [PubMed: 23523780]
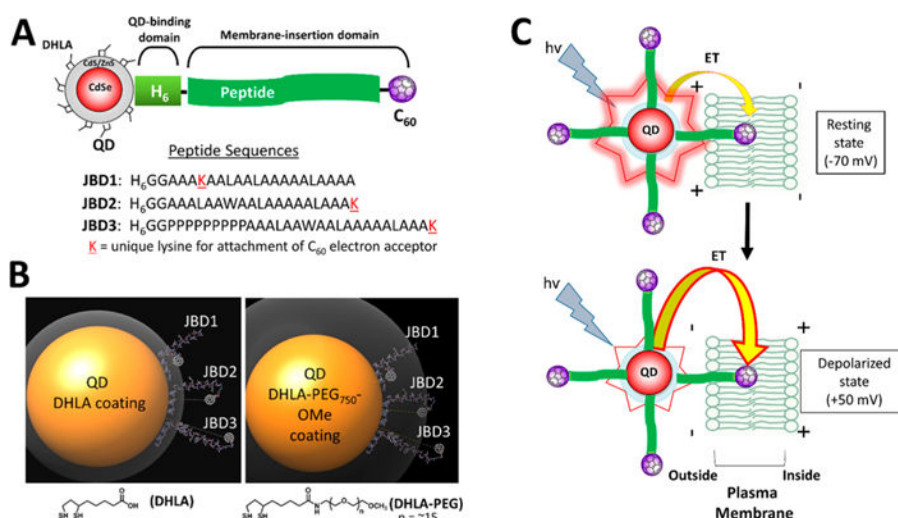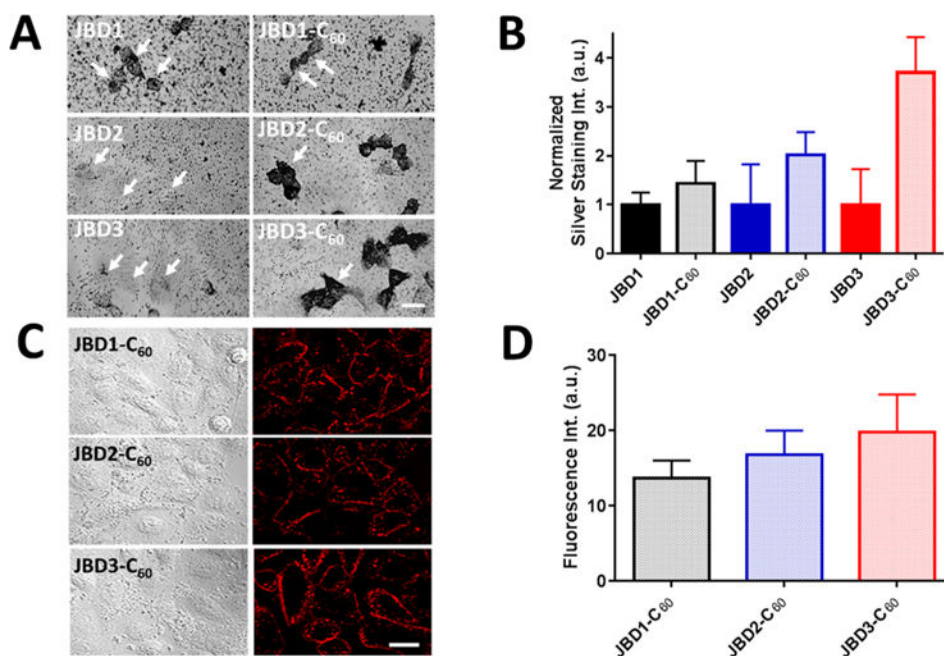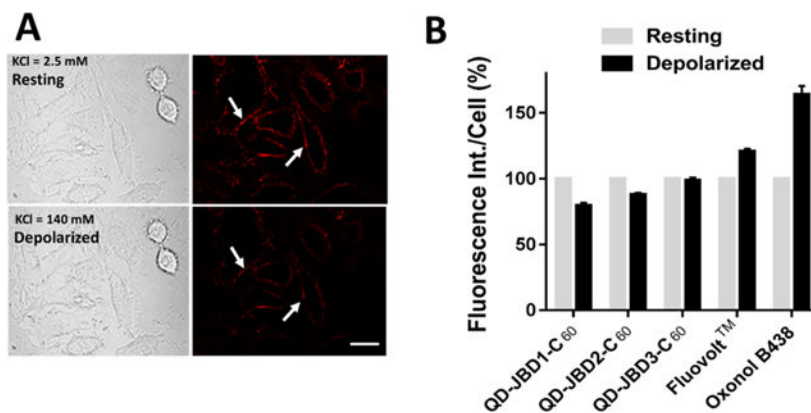
Figure 1.

QD–peptide–C_{60} bioconjugates. (A) Modular design of QD–peptide–C_{60} bioconjugates. The core/shell QD serves as a central scaffold to which is appended peptides bearing a C_{60} fullerene at discrete positions. A unique lysine (K) allows for the controlled placement of the C_{60} moiety at different distances from the QD surface. An N-terminal polyhistidine tract (H_6) mediates self-assembly of the peptide to the QD shell. Peptide sequences are written in N → C orientation. (B) Molecular models of QD–peptide–C_{60} bioconjugates. Shown is the 605 nm emitting core/shell QD (yellow sphere; 100 Å in diameter) capped with DHLA (left panel) and DHLA–PEG_{750}–OMe (right panel) ligands for water solubility. The ligand layer is shown in gray and is 11 Å (DHLA) or 33 Å thick (DHLA–PEG_{750}–OMe). Each QD is shown appended with peptides JBD1, JBD2, and JBD3 wherein the C_{60} electron acceptor is iteratively positioned at increasingly further distances from the QD surface. The predicted surface-to-surface distances from the QD to the C_{60} surface are as follows: JBD1, 10 Å; JBD2, 24 Å; JBD3, 42 Å. (C) Schematic of the response of QD–peptide–C_{60} bioconjugates to changes in membrane potential. Multiple peptide–C_{60} conjugates are arrayed around the central QD (electron donor), and they all engage in electron transfer (ET) with the QD; a percentage of the arrayed peptide–C_{60} are inserted into the membrane bilayer and contribute to depolarization-induced PL quenching. At resting potential, minimal ET from the photoexcited QD to those C_{60} embedded in the membrane bilayer results in bright QD emission (top). Depolarization of the membrane potential augments the rate of ET, causing a decrease in QD PL (bottom).
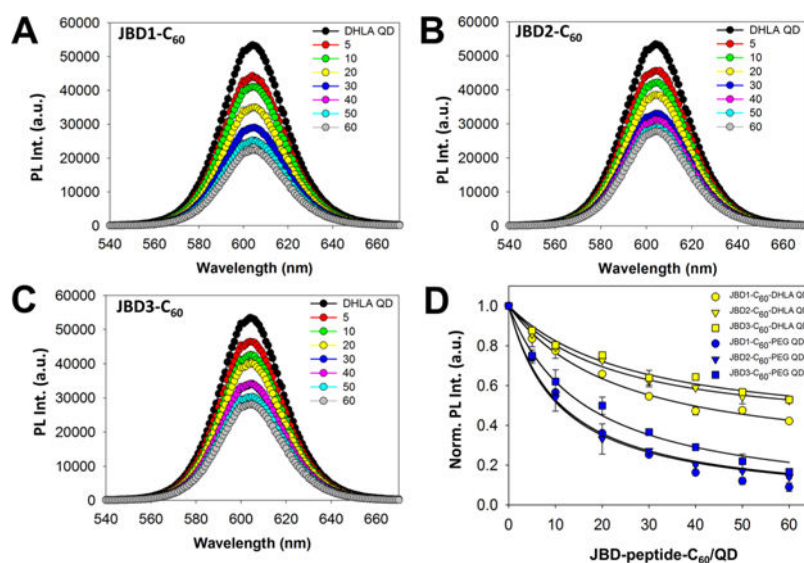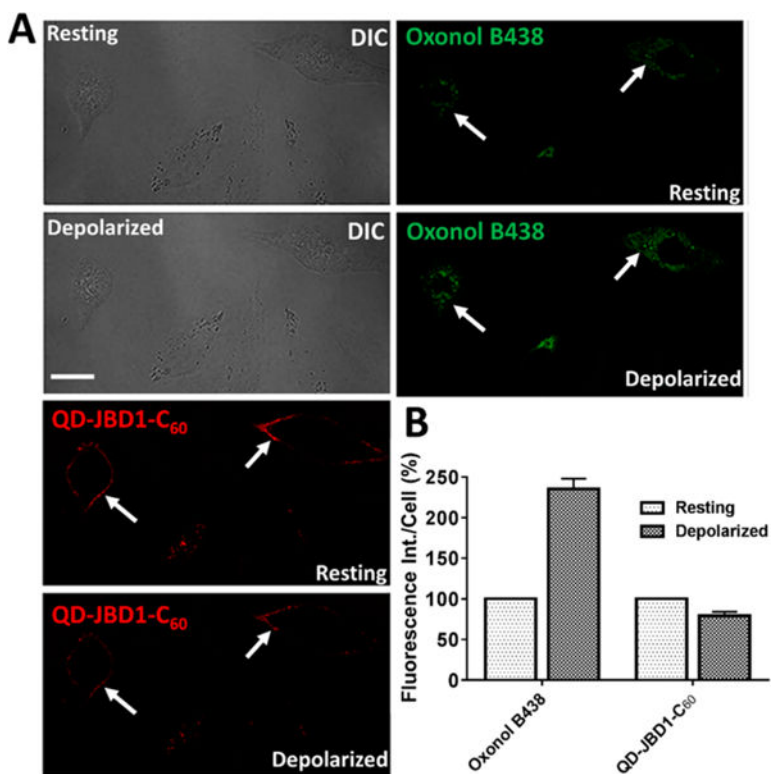
Figure 2.
Steady-state PL analysis of QD–peptide–C_{60} conjugates. Representative PL spectra collected from 605 nm emitting DHLA-coated QDs assembled with increasing ratios of (A) JBD1-C_{60}, (B) JBD2-C_{60}, and (C) JBD3-C_{60} peptides. (D) Comparison of steady-state QD PL (normalized) from QD–JBD–C_{60} conjugates versus increasing ratio of peptide assembled per QD for DHLA–and DHLA–PEG_{750}–OMe-coated QDs.

Figure 3.
Membrane binding of JBD peptides, JBD–C_{60} peptide conjugates, and QD–DHLA–peptide–C_{60} conjugates. Immunocytochemistry combined with silver staining was used to visualize gold nanoparticle-bearing immunoplexes in A549 cells. (A) Cells were incubated with 10 μM JBD peptide minus C_{60} (left column) or 10 μM JBD peptide–C_{60} conjugate (right column), fixed/permeabilized, immunoprobed, and silver stained for the presence of the C_{60} moiety. White arrows point to individual cells. Scale bar, 20 μm. (B) Comparative quantitative analysis of silver stain intensity of the images shown in A. Silver stain intensity was quantified by treating individual cells in each image as separate regions of interest (ROIs). The bar graph shows the resulting average ± SEM of silver stain intensities corresponding to at least 40 cells for each sample (three independent experiments). (C) DIC (left) and confocal fluorescence (right) images of A549 cell monolayers labeled with 605 nm QD–DHLA–JBD peptide–C_{60} complexes as indicated. The micrographs show robust binding of the QD–peptide–C_{60} conjugates to the plasma membrane. Scale bar, 20 μm. (D) Quantification of membrane staining of the QD–peptide–C_{60} QD complexes in panel C. Fluorescence intensities were determined by drawing an ROI around the plasma membrane of individual cells. Bar graph shows the average ± SEM fluorescence intensities of 50 to 70 cells for each sample from four independent experiments. The results shown are background corrected for nonspecific binding of QD alone (no peptide).
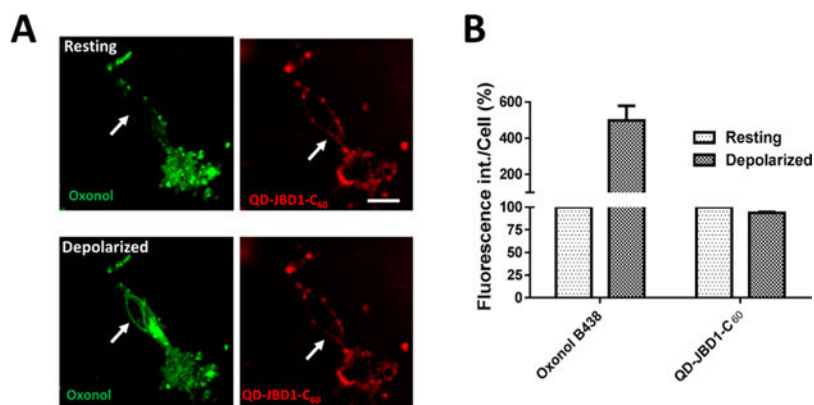
Figure 4.
Imaging of membrane potential changes in cells labeled with QD–DHLA–JBD peptide–C_{60} bioconjugates. (A) Differential interference contrast (DIC) and confocal fluorescence images of HeLa cell monolayers labeled with 605 nm QD–DHLA–JBD1 peptide–C_{60} bioconjugates before (top) and after (bottom) depolarization with KCl solution. Labeled cell monolayers were cultured in live cell imaging solution (LCIS) containing 2.5 mM KCl (resting, top). Depolarization of membrane potential was performed by addition of LCIS containing 140 mM KCl (depolarized, bottom). Scale bar, 20 μm. Arrows highlight the same cell in each panel. (B) Quantification of the fluorescence intensity decrease from resting (2.5 mM KCl, gray bar) to depolarized (140 mM KCl, black bar) membrane potential for the QD–peptide–C_{60} conjugates. The fluorescence response increase of the commercial VSDs FluoVolt and oxonol B438 are shown for comparison.
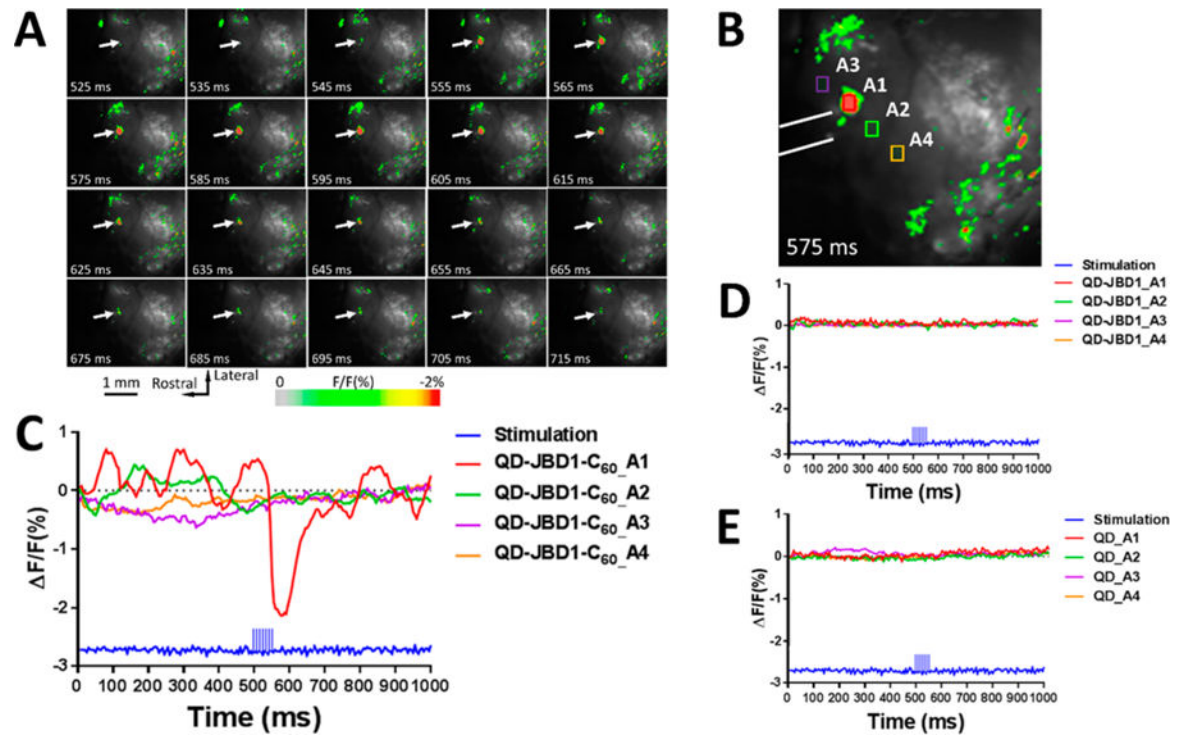
Figure 5.
Dual-channel mode imaging of cellular membrane potential in HeLa cells using QD–JBD peptide–C_{60} bioconjugates and oxonol. (A) HeLa cells were colabeled with 605 nm QD–DHLA–JBD1–C_{60} conjugates (red) and oxonol B438 (green) and were depolarized by KCl perfusion. Shown are the DIC and confocal fluorescence images of HeLa cell monolayers before and after depolarization with KCl solution. Scale bar, 20 μm. White arrows highlight the same cell in each panel. (B) Quantification of the relative change in the fluorescence intensity of the QD–peptide–C_{60} complexes and oxonol upon addition of KCl solution. Fluorescence intensity of the cells was obtained by drawing the ROI around individual cell plasma membranes, and the results represent the mean ± SEM fluorescence intensity of 26 cells for each channel across three separate experiments.

Figure 6.
Dual-channel mode imaging of cellular membrane potential in primary mouse neuronal cells using QD–JBD peptide–C_{60} bioconjugates and oxonol. (A) Confocal fluorescence images of primary mouse cortical neurons colabeled with QD–DHLA–JBD1–C_{60} (red) and oxonol (green) before (top) and after (bottom) KCl perfusion. Scale bar, 20 μm. White arrows denote the same spot in cells pre- and post-depolarization. (B) Quantification of the relative changes in the fluorescence intensity of the QD–JBD1–C_{60} complexes and oxonol upon addition of KCl solution. Fluorescence intensity of the cells was obtained by drawing ROIs around individual neuron membranes. The graph shows the average fluorescence intensity ($\pm$SEM) obtained from 39 cells from five independent experiments.

Figure 7.

In vivo optical imaging of cortical electrical stimulation using QD–JBD1–C_{60} bioconjugates. (A) Images of mouse cortex injected with QD–JBD1–C_{60} conjugates during electrical stimulation. Images were captured at 200 Hz frame rate, and numbers indicate the acquisition time point. Arrow points to ROI A1 shown in panel B; image is false-colored to correspond to scale at bottom. (B) Frame at 575 ms shows fluorescence response of four ROIs. White lines show the position of the bipolar tungsten electrode. (C) Time-resolved fluorescence response of the four ROIs in B showing the averaged response of 50 trials. Panels D and E show the responses of four ROIs in mouse cortex injected with control samples QD–JBD1 peptide (no C_{60}) (panel D) and QDs alone (panel E).